A novel Soft Tissue-Integrated Kinematic Solver for skeletal motion: Validation and applications

K. Duquesne[a, b], A. Van Oevelen[a,b], J. Sijbers[c], W. Van Paepegem[d], E. Audenaert[a,b,e,f]

Affiliations

[a] Department of Orthopedic Surgery and Traumatology, Ghent University Hospital, Corneel Heymanslaan 10, 9000 Ghent, Belgium.

[b] Department of Human Structure and Repair, Ghent University, Corneel Heymanslaan 10, 9000 Ghent, Belgium.

[c] Imec—Vision Lab, Department of Physics, University of Antwerp, 2610 Antwerp, Belgium

[d] Department of Materials, Textiles and Chemical Engineering, Faculty of Engineering and Architecture, Ghent University, Tech Lane Ghent Science 46, 9052 Ghent, Belgium

[e] Department of Electromechanics, Op3Mech research group, University of Antwerp, Groenenborgerlaan 171, 2020 Antwerp, Belgium

[f] Department of Trauma and Orthopedics, Addenbrooke's Hospital, Cambridge University Hospitals NHS Foundation Trust, Hills Road, Cambridge, CB2 0QQ, UK

Corresponding Author: Kate Duquesne, Department of Orthopedic Surgery and Traumatology, Ghent University Hospital, Corneel Heymanslaan 10, 9000 Ghent, Belgium. kate.duquesne@ugent.be

Abstract

Background and Objective:

Kinematic solvers for human motion analysis, relying on oversimplified joint definitions, face inherent limitations in capturing the true spectrum of skeletal motion. Recent advancements incorporated soft tissue constraints to derive more realistic joint kinematics. However, these methods require marker data input and are computationally expensive, limiting their application to specific joints. This paper proposes a novel kinematic solver that addresses this gap by explicitly accounting for soft tissues, while allowing for accurate and computational efficient modeling across diverse movements and joints.

Methods:

The proposed soft tissue-integrated kinematic solver determines the kinematics by relying on the principle of force balance. In a cascaded iterative way, the position and orientation of each individual segment is updated by minimizing the force residual acting on the segment The latter is solved through a unique way by defining and aligning two point clouds. Accuracy was assessed with three datasets: in-vivo MRI squats (N=9), in-vitro cadaver CT squat (N=1), and in-vitro cadaver arm flexion/extension/pro-supination (N=1). The accuracy was assessed by computing the absolute error on the joint angles and translations and benchmarked against traditional inverse kinematics with a revolute joint as well as two computer vision techniques (OSSO and SKEL).

Results:

All experiments showed that with sufficient input data (over 5 rigid bone markers, or skin zones), the primary motion error was almost without exception under 1.5°. This outperformed the inverse kinematics with revolute joint (7.29° flexion-extension), OSSO (9.59° flexion-extension) and SKEL (3.19° flexion-extension) methods. The median error on the secondary kinematics for the humeroulnar and ulnoradial joints were below 3.78° and 2.50 mm when driving the motion with skin zones. For the tibiofemoral joints, errors were under 5.39° and 3.5 mm. Computation time was below 30 seconds per frame.

Conclusions:

The kinematic solver enables exploring all degrees of freedom accurately without compromising computational efficiency. Unlike biomechanical methods which are limited to marker data, the kinematic solver can analyze both marker and skin data.

Keywords: Kinematic solver; Soft-Tissue Modeling; Computational Modeling; Knee Joint; Elbow joint; Motion Analysis

1. Introduction

The exploration of human motion analysis dates back to the early 1800s. Over the years, diverse methodologies have evolved for its examination, ranging from simple goniometry over manual identification of landmarks on images/video frames to the application of sophisticated kinematic solvers [1]. The traditional kinematic solvers assume that the body is a series of rigid segments connected by idealized – limited Degree Of Freedom (DOF)- joints without considering any soft tissue structures [2], [3], [4], [5]. For example, the hip and intervertebral joints are typically modelled as spherical joints, the knee joint as a revolute joint and the ankle and subtalar joints as two nonorthogonal revolute joints (Table 1). While this assumption is suitable to approximate simple motions such as walking and for applications in which the accuracy of the determined kinematics is not of high importance, it proves inadequate when modeling the kinematics and dynamics of joints in clinical settings or for more complicated movements in (sport) biomechanics [6], [7]. This inadequacy arises because the majority of anatomical and prosthetic joints are nonconforming, causing to significantly influence the joint's (secondary) kinematics and internal force equilibrium [8], [9]. Further, the contribution and deformation in the involved soft tissue structures such as cartilage, muscles, tendons and ligaments are not accounted for. Yet, these structures not only serve as connections between rigid skeletal elements but also play an important role in shaping and guiding the resulting kinematics [9], [10], [11].

Numerous efforts have been undertaken to develop more reliable kinematic solvers, in both commercial and open-source frameworks (Table 1). For example, Andersen et al. presented Force Dependent Kinematics (FDK), a technique that concurrently optimizes muscle, ligament, and joint contact forces alongside secondary kinematics, i.e. the non-primary motion of a joint [12], [13]. Similarly and specifically for the knee, several researchers have augmented the conventional OpenSim gait model by incorporating soft tissue constraints, allowing for a six-degree-of-freedom tibiofemoral joint to better replicate the true

knee joint motion [14], [15], [16]. While these methods demonstrated significant potential, they have a higher computational cost compared to traditional methods using simplified joints. Additionally, they require a greater number of additional parameters, both subject-specific and model-related, and therefore typically their implementation is confined to a single joint of interest.

Beyond the complexities of improving the numerical approaches for joint kinematics, soft tissue artifacts (STAs) remain an additional and significant challenge in marker-based motion analysis. These artifacts arise from the movement of the skin and the underlying tissues relative to the bony landmarks, leading to inaccuracies in joint angle calculations. To mitigate STAs and enhance the accuracy of kinematic analysis, several STA compensation methods have been proposed. Examples include strategic marker placement at locations where STAs are anticipated to be minimal and the use of marker clusters [17]. Additionally, various computational methods, such as filtering, multibody kinematics optimization and co-registration with other imaging modalities, have been developed to mitigate the impact of STAs [7], [18], [19], [20], [21], [22], [23], [24]. The multibody kinematics optimization techniques incorporate other factors such as constraining degrees of freedom within adaptive boundaries, projecting the skin markers onto a selected axis of the local system of coordinates to cancel the deleterious effect of STA on that specific degree-of-freedom or incorporating Finite Element (FE) models[7], [18], [19]. More recently, Einfeldt et al. presented a novel technique to minimize knee soft tissue artifacts [20]. Their method employs frame-by-frame optimization to refine best-fit cylinders that are initially generated based on the relative positions of lower limb markers during a static trial. Tibiofemoral rotations and translations are subsequently calculated along the anatomical joint axes using the relative 3D motion of these cylinders. Similar to the advanced kinematic solvers in the previous paragraph, these solutions have a higher computational cost and are often confined to one specific joint of interest.

In contrast to the above mechanical approaches which focus on numerical modelling of the skeletal structures to define joint kinematics, computer vision techniques have been developed to accurately

represent the body's surface and thereby infer approximative skeleton kinematics based on skin movements (Table 1) [25], [26], [27]. These techniques use a kinematic tree, often a simplified 'stick figure' with spherical joints, to represent the skeleton [25], [26], [27]. The obtained joint angles are, therefore, not suitable for clinical or biomechanical applications. Two recent methods, Obtaining Skeletal Shape from Outside (OSSO) and Skeletal Kinematics Enveloped by a Learned body model (SKEL), aim to address this oversimplification [28], [29]. Both OSSO and SKEL infer a more realistic skeleton directly from the skin surface, approximating both its shape and position. Once the skeletal shape and position are estimated, joint angles can be calculated using the anatomical correspondence inherent in the reconstructed skeletons and biomechanical standards. OSSO, trained on dual-energy X-ray absorptiometry (DXA) scans with subjects in a supine position, uses a three-step process: repositioning the skin mesh to a standardized lying down position, inferring the skeleton, and repositioning the estimated skeleton with pre-defined physical constraints (enforcing skeletal coherence, maintaining ball joint distances, and simulating knee ligament behavior through energy terms). However, repositioning the skeleton requires an optimization process that sometimes results in biomechanically impossible poses e.g. extreme joint displacements or mesh penetrations. SKEL, on the other hand, leverages an idealized biomechanical skeleton, created within the OpenSim framework, to re-rig a parametric skin mesh called 'SMPL' (Skinned Multi-Person Linear Model). This biomechanical skeleton, with its 24 segments, is essentially scaled and positioned within the SMPL mesh. Importantly, the skeleton does not incorporate soft tissue constraints such as ligaments or cartilage.

Marker-based motion analysis	Markerless motion analysis
Traditional kinematic solvers	**Computer vision techniques**
• Skeleton represented as a series of rigid bodies (segments) • Segments are connected with simplified joints chosen to match the primary motion of the corresponding joint	• Skeleton represented as a stick figure, which does not necessarily align with the real skeleton • Segments are connected with simplified joints (typically spherical joints)
Advanced kinematic solvers	
• Skeleton represented as a series of rigid bodies (segments) • Take into account the contribution of soft tissue structures using a force balance • Require a greater number of parameters and have increased computational cost • The implementations are often confined to a single joint of interest	
Soft tissue-integrated kinematic solver	
• Skeleton represented as a series of rigid bodies (segments) • Works with both bone/skin markers and the skin input • No restrictions on the joint angles and translations • Takes into account the contribution of soft tissue structures using two corresponding point clouds as force balance analogy • Novel concept to solve the positioning of the segments based on aligning point clouds using Singular Value Decomposition • Without compromising computational efficiency	

Table 1: An overview highlighting the main characteristics of the marker-based and markerless motion analysis methods. The proposed methodology works with both marker-based and skin (markerless) input.

In summary, no current complete skin based method can fully capture the complex interplay between muscles, contact forces, and ligaments to measure realistic joint movements using the skin as input.

Hence, this paper addresses this critical gap in kinematic modeling by introducing a new kinematic solver designed to account for the soft tissue constraints. Unlike conventional biomechanical methods that explicitly define joints between neighboring segments, this approach operates on segment definitions. In this method, the segments are connected to the neighboring segments using only soft constraints instead of hard joint constraints. The latter enables all degrees of freedom to be freely explored without compromising computational efficiency. Additionally, the solver can analyze both marker and skin data, unlike biomechanical methods which are limited to marker data and computer vision approaches that rely on body scan meshes.

2. Materials and methods

This section begins by outlining the general principles underlying the proposed soft tissue-integrated kinematic solver. The developments outlined in this paper have been filed in a patent application. Subsequently, the performance of the kinematic solver was assessed through three distinct experiments: (1) an in-vivo experiment on the knee joint with healthy volunteers in an MRI setting, (2) an in-vitro experiment on a cadaver knee joint using CT imaging and (3) an in-vitro experiment with a cadaver elbow joint in a CT scanner. An overview of the article structure is presented in Figure 1.

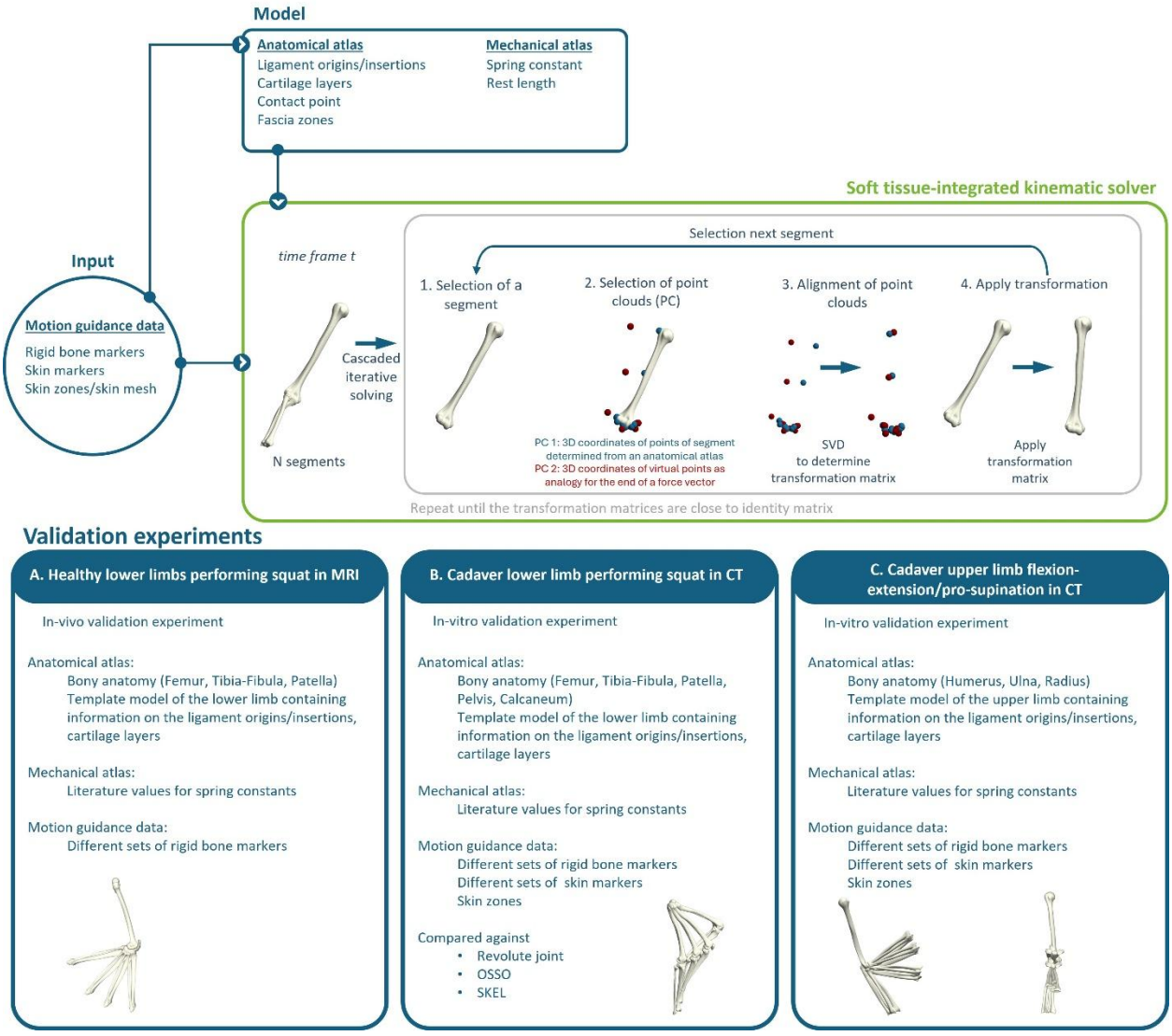

Figure 1: An overview of the article structure, starting with the general concept and implementation of the kinematic solver, followed by the application of the kinematic solver in three use cases (A - C) for validation purposes including an illustration of the ground truth bony positions.

2.1. Technical description of the 'Soft tissue-integrated kinematic solver'

2.1.1 General concept

The soft tissue-integrated kinematic solver determines the skeletal kinematics by operating on segment definitions. The soft tissue-integrated kinematic solver requires the system (i.e. the skeleton or body and

144 the markers/skin mesh) to be defined by an user-defined anatomical, stored as dictionaries, and
145 mechanical atlas and experiment dependent motion guidance data (Figure 2). The atlases are stored as
146 dictionaries in Matlab.

147 - *The anatomical atlas* contains relevant anatomical information and experiment-dependent bone
148 and skin marker data (i.e., all ligament/muscle origins and insertions on the segment, cartilage
149 layers on the segment, contact points on the segments with the neighboring structures and fascia
150 zones (zones were the fascia is close to the bony surface))
151 - *The mechanical atlas* includes mechanical properties of ligaments and contacts, as well as
152 experiment-dependent mechanical data for bone, skin markers, and skin connections (i.e. the
153 spring constants and rest lengths for ligaments and contacts)
154 - *The motion guidance data* encompasses various motion data types, namely rigid bone markers –
155 marker attached to a fixed point on the bone-, skin markers or skin zones – specific areas on the
156 skin meshes selected for their informative value in capturing bone movements- depending on the
157 experiment (Figure 3).

158 The skeleton is represented with N rigid segments, each having 6 degrees of freedom (3 translations and
159 3 rotations). This cumulates to a total of 6*N degrees of freedom for the entire skeleton. The individual
160 segments are extracted from a full body mesh template. Here, this template mesh has an edge length of
161 1.5mm. At its core, the soft tissue-integrated kinematic solver relies on the principle of force balance. To
162 do so, each individual segment is connected to the environment (i.e. neighboring segments, bone/skin
163 markers and the skin mesh) through springs. For every segment, the springs and their respective forces
164 are determined from the anatomical atlas, the mechanical atlas and the motion guidance data. In the
165 anatomical atlas all anatomical relevant data is summarized (i.e., all ligament/muscle origins and insertions
166 on the segment, cartilage layers on the segment, contact points on the segments with the neighboring
167 structures and fascia zones (zones were the fascia is close to the bony surface)) for every rigid segment.

Similar to the anatomical atlas, the mechanical atlas defines all mechanical relevant data (i.e. the spring constants and rest lengths for ligaments and contacts). The rest lengths of the ligaments are determined in a specific joint position where the ligament length is equal to the ligament rest length or is determined by computing the rest length based on a known ligament strain in a certain joint position. The rest length of the contacts are defined to be zero. Finally, the soft tissue-integrated kinematic solver requires motion guidance data. This can either be rigid bone markers, skin markers or skin zones can be used, depending on the experiment. Similar to the ligaments and contacts, the motion guidance data are represented in the solver using springs between the marker position and the corresponding point on a segment. For the skin zones, for every point located within the designated skin zones on the skin mesh, a corresponding spring is generated. The bone and skin marker locations and the locations of their corresponding points on the segments are incorporated into the respective user-defined anatomical atlases. The skin markers and corresponding skin zones, which correspond to specific points on the segments, are identified in the initial frame of motion by conducting a k-nearest neighbors search between pre-defined points on the segments and the skin surface. Additionally, spring constants and rest lengths are defined for these marker interactions and added to the user-defined mechanical atlas. The rest lengths are determined in the first frame of motion, which in the validation experiments corresponds to the leg/arm in the straight position.

Once the necessary, anatomical and mechanical data are compiled into their atlases which describe the system, the soft tissue-integrated kinematic solver can be employed to determine the positions of segments in a cascaded iterative loop. For a specific time frame, first, a segment is selected (Figure 2 (1)). For this segment, each interaction (ligament, contact, or marker/skin) between the segment and the neighborhood are modelled as springs. However, for its calculation the kinematic solver leverages on point clouds. In other words, the solver defines a pair of points as analogy of a spring, one point in each point cloud. The first point cloud consists of the 3D coordinates of points located on the surface of the selected segment and describes the current position of the selected segment (Figure 2 (2a)). These include the 3D

coordinates of the ligament origins and insertions ON the segment, the 3D coordinates of the contact points with neighboring structures ON the segment and the 3D coordinates of the points ON the selected segment corresponding to the skin and/or bone/skin markers, defined from the anatomical atlas from the selected segment.

The second point cloud or so called ‘Force cloud’ encodes for the forces exerted on the segment by its neighboring structures (Figure 2 (2c)). The larger the exerted force, the further the distance from the point in the force cloud to the corresponding point in the first point cloud. This relationship is described by a non-linear equation, typically used to model ligament behavior [30]. The same relationship is used for all three types of constraints, i.e. ligaments, contacts and rigid bone/skin markers and skin. Subsequently, to minimize the force residual acting on the segment, the transformation matrix to rotate and translate the segment that minimizes the sum of squared errors between the rotated and translated point cloud and the force cloud are determined (Figure 2 (3)). This transformation matrix is then applied to the selected segment (Figure 2 (4)). The solver proceeds segment by segment in a cascaded but independent fashion. In each iteration, the position of a selected segment is updated and immediately stored in a temporary 'skeleton updated' structure. This ensures that the update of one segment's position is not influenced by the updated positions of its neighbors within the same iteration. Once all segment positions have been updated independently and stored, the complete 'skeleton updated' structure replaces the previous skeleton state, and a new iteration can begin. Unlike in traditional biomechanics methods, there is no need for a base segment to keep the skeleton grounded. This iterative refinement is repeated until all the transformations converged to the identity transformation before continuing to the next time frame.

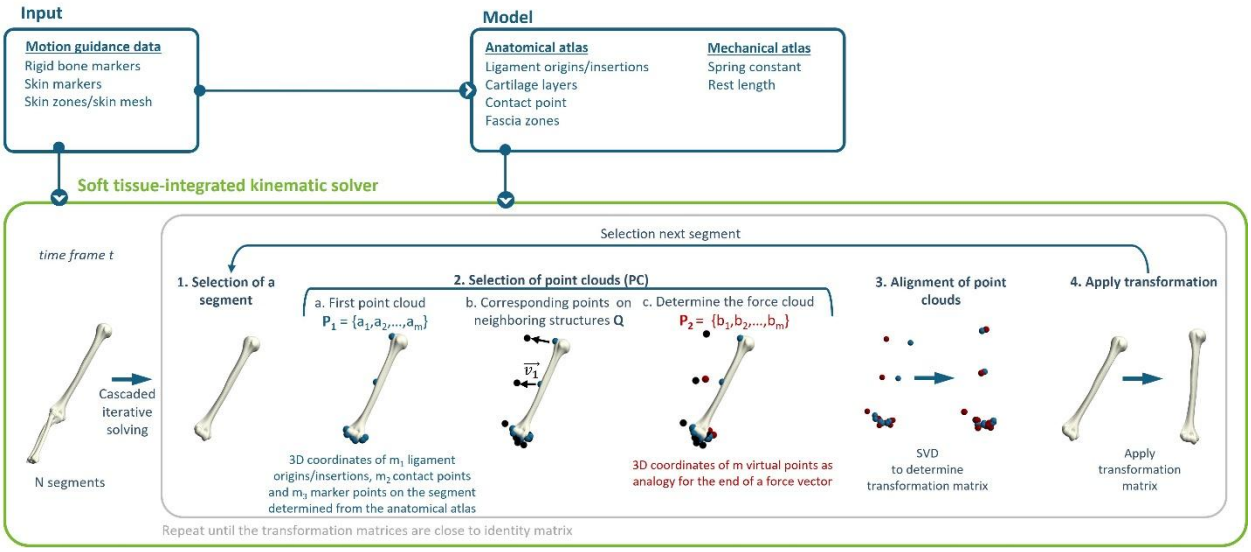

Figure 2:The workflow of the soft tissue-integrated kinematic solver. In every frame, the position and orientation of every segment is updated in a cascaded manner until convergence before moving to the next frame. Focusing on a single iteration of the solving process, a particular segment is chosen for examination and is labeled as the 'selected segment' (1). In every iteration, a point cloud and a force cloud are identified. In the example, the selected segment has m_1=4 ligament connections, m_2=5 (joint) contact connections with neighboring structures and m_3=4 skin marker connections. By exploiting the anatomical atlas, the first point P_1 cloud comprises of 4 coordinates of the ligament origins, 5 coordinates of contact points on the segment and 4 coordinates of points on the segment corresponding to the skin markers (2a). Next, the corresponding points on the neighboring segments and skin are derived from the anatomical atlas (2b). Thereafter, between the first point cloud P_1 and the corresponding point cloud Q 13 virtual springs are drawn. From the current length of the spring, and the data from the mechanical atlas, the 3D coordinates from the points in the force cloud P_2 are determined (2c). Subsequently, the force balance is solved by determining the transformation that minimizes the sum of squared errors between the corresponding point clouds P_1 and P_2 (3). Finally, this transformation is applied to the selected segment (4).

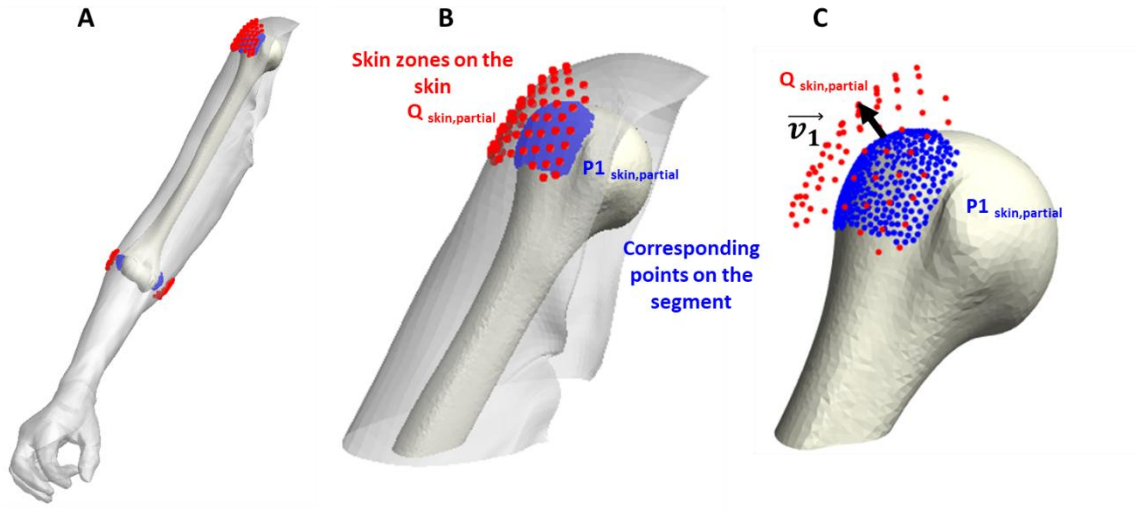

227

228 *Figure 3: An example of skin zones: the selected segment, i.e. the humerus, is plotted together with the*
229 *skin and the skin zones (A). The red dots indicate the points on the skin which are part of the skin zones*
230 $Q_{skin,partial}$*. These points are part of point cloud Q. The blue dots* $P1_{skin,partial}$ *indicate the* m_3 *points on the*
231 *humerus corresponding to the skin zones on the segment (B). The latter will be part of point cloud* P_1*. One*
232 *vector* $\overrightarrow{v_1}$ *from the* $P1_{skin,partial}$ *to* $Q_{skin,partial}$ *is drawn (C). In the example, the skin has a lower resolution mesh*
233 *than the bone mesh, as a consequence, in this example multiple vectors will end in the same node on the*
234 *skin.*

235 **2.1.2 Implementation**

236 Building on the above concept, this paragraph will delve deeper into the implementation of the novel soft
237 tissue-integrated kinematic solver. In a single iteration of the solving process, a particular segment is
238 chosen to update its position and orientation and is labeled as the 'selected segment' (Figure 2(1)). To
239 update its position, an isolated force balance is computed. This means we analyze one segment at a time
240 and minimize the force residual acting on it. To do so, two point clouds of m corresponding points are
241 defined (Figure 1).

First point cloud

The first point cloud $P_1(\{a_1, a_2, \dots, a_m\})$ is composed of m ($m = m_1 + m_2 + m_3$) 3D coordinates derived from the anatomical atlas and can be divided into three groups (Figure 2(2a)). The first point cloud:

1. contains m_1 3D coordinates of the ligament/muscle origins and insertions on the segment.
2. includes the m_2 3D coordinates of the contact points with the neighboring segments. Unlike the ligaments which have fixed origin and insertion locations on the segments, the contact points between the segments are not fixed. Instead, the solver has one fixed contact point on the concave side of the joint, whereas the contact point on the convex side is determined for each segment configuration. The solver identifies the closest point on the convex articulating surface while considering the surface normals at the articulating zone. The kinematic solver uses a nearest neighbor search to identify point in the convex cartilage layer that are close to and with a normal in the opposite direction to a fixed contact point on the concave surface.
3. comprises the m_3 3D coordinates of the (marker) contact points on the segment with the skin zones or with the rigid bone markers. Similar to the ligaments, these points have fixed locations on the segments.

Second point cloud: Force cloud

To restate, during each iteration of the solver, the selected segment is virtually connected to the environment (i.e. neighboring segments, bone/skin markers and the skin) through (straight) springs. Their respective forces are determined from the anatomical atlas, the mechanical atlas and the motion guidance data. To address the challenge of balancing forces, a new method has been developed to achieve equilibrium within the interactions. To do so, the second point cloud or so called 'Force cloud' $P_2(\{b_1, b_2, \dots, b_m\})$ is introduced (Figure 2 (2c)). The force cloud is a virtual point cloud of an equal number of m points and encodes for the forces exerted on the segment by its neighboring structures. To obtain the 3D coordinates of these points, a point cloud Q is initially specified, comprising the 3D coordinates of

ligament origins and insertions on neighboring segments, 3D coordinates of contact points on the neighboring segment, and 3D coordinates of measured bone/skin markers in 3D space or skin zones on the skin mesh (Figure 2 (2b)). The points of the second point cloud are positioned on the vector $\vec{v} = Q - P1$ between the points of the segment under investigation P_1 and the corresponding point on the neighboring segment Q (Equation 1-5).

More specifically, first the vector $\vec{v}$ is normalized ($\vec{w} = \frac{\vec{v}}{\|\vec{v}\|}$). Next, for each group (i.e. group 1: ligaments/muscles, group 2: contact, group 3: bone/skin marker and skin contact), the spring constants (k) are normalized by dividing it with the maximal spring constant of each group (Equation 1-3). Next, for the ligaments the 3D coordinates of the points in the force cloud are determined using equation 4 and 5. To balance the influence of different constraint types, the spring constants (k) for contact and bone/skin marker contact are normalized with the spring constant of the ligaments. This is achieved by multiplying the original spring constants by the ratio between the sum of all the ligaments spring constants to the sum of all the contact/bone-skin marker spring constants (Equation 2-3). To balance between different constraint types (i.e. ligaments, contact and markers), a scaling parameter is additionally applied ($\lambda_{type\ of\ constraint}$). The standard values for $\lambda_{ligament}, \lambda_{contact}$ and $\lambda_{marker/skin}$ are 1,1 and 1.

$$k_{lig}^{*} = k_{lig} / \max\left(k_{lig}\right) \quad (1)$$

$$k_{contact}^{*} = \frac{k_{contact}}{\max(k_{contact})} \cdot \frac{\sum k_{lig}^{*}}{\sum k_{contact} / \max(k_{contact})} \quad (2)$$

$$k_{marker/skin}^{*} = \frac{k_{marker/skin}}{\max(k_{marker/skin})} \cdot \frac{\sum k_{lig}^{*}}{\sum k_{marker/skin} / \max(k_{marker/skin})} \quad (3)$$

With k_{lig}, $k_{contact}$ and $k_{marker/skin}$ the spring stiffness of the ligaments, contacts and rigid bone/skin or skin zones and k_{lig}^{*}, $k_{contact}^{*}$ and $k_{marker/skin}^{*}$ the normalized spring contacts of the ligaments, contacts and rigid bone/skin or skin zones.

$$P_2 = P_1 + \lambda_{type\ of\ constraint}\, d.\vec{w} \quad \text{with } d \leq 1 \tag{4}$$

With P_1 and P_2 (size mx3) the 3D coordinates of the points in respectively point cloud 1 and the force cloud, w (size mx3) the normalized vector between the corresponding points on the selected segment and the neighboring segment, d (size mx1) distance along vector $\vec{w}$ and $\lambda_{type\ of\ constraint}$ (size mx1) a scaling parameter to control the balance between different constraint types.

The distance d along the vector is defined by a non-linear relationship comprising the ligament/contact properties and the ligament/contact strain (Equation 5) [30].

$$d = \begin{cases} 0 & \varepsilon < 0 \\ k^*.(d_{initial} - L_0)/2 & 0 \leq \varepsilon \leq 2.\varepsilon_l \\ k^*.(d_{initial} - (1+\varepsilon_l).L_0) & 2.\varepsilon_l < \varepsilon \end{cases} \tag{5}$$

With d distance along vector $\vec{w}$ in equation 4, $d_{initial}$ the length of the vector $\vec{v}$, L_0 the rest length of the ligament, contact or marker/skin contact, k^* the normalized spring constant of the ligament, contact, marker/skin contact, ε_l threshold strain, which indicates the change from the toe to the linear regions in a stress/strain curve, ε the engineering strain defined by $\frac{d_{intitial} - L_0}{L_0}$ and L the length of the ligament, contact or marker/skin contact. For simplicity, we assumed a threshold strain of 0.03 for all ligaments [31].

As final remark, when using the entire skin or specific skin areas to guide movement, the system verifies the direction of the vector ($\vec{v}$) to prevent the segment from penetrating the skin.

Force balance – Determine the transformation matrix

As final step of a single iteration of the soft tissue-integrated kinematic solver an isolated force balance is computed. In other words, we minimize the residual of the force equilibriums. This is done through a force balance analogy. By aligning the previously defined point cloud with the force cloud, we solve the force balance problem. More specific, the transformation matrix to rotate (T (size 3x3)) and translate (c (size

1x3)) the segment that minimizes the sum of squared errors between the rotated and translated point cloud and the force cloud is determined (Equation 6, Figure 2(3)).

$$Determine\ (T, c)\ \ so\ that\ it\ minimizes\ \ (P_2 - (P_1.T + c))^2 \quad (6)$$

With P_1 and P_2 (size mx3) the points in respectively point cloud 1 and the force cloud, T a rotation matrix of size 3x3 and c the translation vector of size 1x3.

The alignment process is based on a Singular Value Decomposition (SVD) and utilizes a sum squared errors (SSE) as goodness of the fit (Equations 7-14). First, the center of the point clouds is determined (Equation 7-8).

$$\mu_{P2} = \frac{1}{m}\sum_{i=1}^{m} P_2 \quad (7)$$

$$\mu_{P1} = \frac{1}{m}\sum_{i=1}^{m} P_1 \quad (8)$$

With P_1 and P_2 (size mx3) the points in respectively point cloud 1 and the force cloud, $\mu_{P1}$and μ_{P2} the mean coordinate in 3D space of respectively the first point cloud P_1 and the force cloud P_2.

Subsequently, the point cloud and force cloud are centered and normalized (Equation 9-10).

$$P_2^* = \frac{P_2 - \mu_{P2}}{\|P_2 - \mu_{P2}\|} \quad (9)$$

$$P_1^* = \frac{P_1 - \mu_{P1}}{\|P_1 - \mu_{P1}\|} \quad (10)$$

With P_1^* and P_2^* (size mx3) the 3D coordinates of the centered and normalized points of respectively point cloud 1 and the force cloud, μ_{P1} and μ_{P2} the mean coordinate in 3D space of respectively the first point cloud P_1 and the force cloud P_2.

Next, the singular value decomposition (SVD) performed on the matrix product of the centered and normalized point clouds (Equation 11).

$$[\mathrm{L}, \mathrm{D}, \mathrm{M}] = SVD\left(P_2^{*T}.P_1^*\right) \quad (11)$$

With P_1^* and P_2^* (size mx3) the 3D coordinates of the centered and normalized points of respectively point cloud 1 and the force cloud, L the left singular vectors, D the singular values and M the right singular vectors.

Following, the rotation matrix that minimizes the sum of squared errors between point cloud 1 and the force cloud is computed form the left and right singular values (Equation 12).

$$T = M.L^T \quad (12)$$

With T the rotation matrix of size 3x3, L the left singular vectors and M the right singular vectors.

Finally, the translation vector is determined from the center of the force cloud and the rotated center of the first point cloud (Equation 13).

$$c = \mu_{P2} - \mu_{P1}.T \quad (13)$$

With c the translation vector of size 1x3, T the rotation matrix of size 3x3, μ_{P1} and μ_{P2} the mean coordinate in 3D space of respectively the first point cloud P_1 and the force cloud P_2.

Subsequently, the determined transformation (T, c) is applied to the selected segment (Equation 14, Figure 2(4))).

$$S_{new\ position} = S_{old\ position}.T + c \quad (14)$$

With $S_{old\ position}$ and $S_{new\ position}$ (size nx3) the selected segment in respectively the old and new position and orientation, T a rotation matrix of size 3x3, c the translation vector of size 1x3, n the number of vertices of the selected segment.

The solver then repeats this process for the other segments of the system. For each selected segment, it determines the new positions and orientations based on the results from the previous iteration. Upon

updating all segment positions, the solver evaluates the proximity of transformations to identity matrices. The proximity to identity matrices is assessed using a threshold on the maximum angular rotation and translation. To do so, the rotation matrix T is decomposed into Euler angles (sequence: ZYX) (α, β and γ) and the Euclidean norm of the translation vector c is computed. Convergence is established when both the maximum rotation angle and the maximum translation error among all segments fall below a defined threshold (Equation 15). Once convergence is achieved, the algorithm advances to the subsequent time frame. Conversely, the process is repeated using the refined segment positions (Figure 2).This soft tissue-integrated kinematic solver was implemented in MATLAB v2023a (MathWorks, Natick, MA, USA).

$$\max([\alpha_1, \dots, \alpha_N, \beta_1, \dots, \beta_N, \gamma_1, \dots, \gamma_N]) < \text{angle}_{\text{threshold}} \,\&\, \max([\|c_1\|, \dots, \|c_N\|\,]) < \text{translation}_{\text{threshold}} \quad (15)$$

With α_1, β_1 and γ_1 and α_N, β_N and γ_N the decomposed Euler angles of the rotation matrix of respectively the first segment and Nth segment, c_1 and c_N the translation vector of the first segment and Nth segment. The $\text{angle}_{\text{threshold}}$ and $\text{translation}_{\text{threshold}}$ represents the maximum permissible rotation angle and translation distance and were respectively set to 10^{-3} radians and to 10^{-5} m in the experiments discussed in section 2.2.

To summarize, this section outlined the general principle of the kinematic solver. In the following sections, the solver is applied in different use-cases (different body parts) and validation experiments to show its capabilities. In these validation experiments, a more detailed overview of the involved anatomical and mechanical atlases is provided.

2.2 Validation experiments

Three validation experiments (one in-vivo and two in-vitro) were conducted using ground truth bone positions obtained from either CT or MRI scans. The soft tissue-integrated kinematic solver's accuracy was measured by the absolute error on the rotations and translations between the ground truth values and

the solver's estimations. The first, in-vivo experiment focused on applying the soft tissue-integrated kinematic solver to the lower limb and assessed its accuracy on the tibiofemoral joint angles and translations. This first experiment (A) employed increasing numbers of rigid bone markers, which offer clean motion data, to establish the optimal marker count for motion analysis in both underdetermined and overdetermined systems. This enabled us to demonstrate the solver's effectiveness in handling movement without skin artifacts or thus under ideal conditions. Considering this experiment involved healthy volunteers, the imaging modality was MRI. Due to the limitations of the Field of View (FOV), the complete skin surface could not be captured. Consequently, only rigid bone markers were employed in this experiment. Further, this experiment was used to illustrate the possibility and effect of optimizing the ligament properties on the solver's performance.

In a second validation experiment (B), an in-vitro experiment involving a cadaver knee, was particularly designed to assess the solver's accuracy using skin zones as input rather than traditional sparse marker data input. CT scans were acquired of the knee joint in various positions mimicking a squat. The performance of the soft tissue-integrated kinematic solver was evaluated on tibiofemoral joint angles and translations.

The final and third validation experiment (C) was designed to assess the soft tissue-integrated kinematic solver capability for joints geometries different from the knee, namely the humeroulnar and radioulnar joints. CT scans were acquired of the elbow joint in a series of positions spanning a large range of motion. All experiments were conducted in accordance with the ethical principles outlined in the declaration of Helsinki and scanning the subjects/cadavers was approved by the ethical committee (reference numbers: B6702021000905 (in-vivo lower limb) and B670201421989 (in-vitro cadaver leg and cadaver arm)). Below a description of every experiment is provided including the anatomical and mechanical atlases and the motion guidance data.

2.2.1. In-vivo validation experiment (A): Healthy Lower Limb performing squats in a MRI scanner

In the first validation experiment, the novel soft tissue-integrated kinematic solver's performance was evaluated on the tibiofemoral joint using rigid bone markers to guide the motion.

Input data and pre-processing

Data from 9 healthy subjects performing loaded lying-down squats during an MRI scan were used. The detailed protocol and overview figure is available in [32]. Each participant underwent MRI scanning with their knee in increasing flexion angles (0°, 30°, 60°, and 90°) while pressing the dominant leg's foot against a wooden bar. A weight of 25 kg, roughly half the body weight, was attached to the leg. High-resolution scans were acquired using a 3 Tesla Vantage Galan Canon® MRI machine. The scans had a pixel size of 0.3571 mm x 0.3571 mm and a slice thickness of 1.5 mm. The femur, patella, and tibia-fibula complex were segmented using Audenaert et al.'s semi-automatic method, resulting in segmentation of dense corresponding surface meshes for each subject [33]. For each subject, a knee flexion motion of 28 frames was created. To do so, Principal Polynomial Shape Analysis (PPSA) was applied on the corresponding meshes in the four available knee configurations and subsequently interpolated [34]. These additional frames ensure the kinematic solver encounters manageable steps during its calculations. Only the four actually measured knee configurations were used for evaluation, not the interpolated ones. Simulated rigid bone marker trajectories were generated by identifying corresponding indices on the registered bony structures, aligning with the bony landmarks. These indices were then used to extract the Euclidean coordinates of the corresponding points throughout the motion.

Anatomical and mechanical atlas

A template model encompassing three segments (femur, patella, tibia-fibula complex), ligament and muscle origin and insertions as well as contact conditions was created (details in Figure 4(A) and Table A.1). The template model considered only the passive elastic properties of the quadriceps muscle, treating

it like a spring to oppose the force exerted by the patellar tendon. Non-rigid registration of this template on the segmented bones mapped the template anatomical information onto the individual subjects' legs. The required landmarks to compute the joint angles were defined by landmark transfer using in-house available statistical shape models [35]. The mechanical information was kept fixed. Given the substantial variability of ligament parameters reported in the literature, fixed spring constants were used. However, the rest lengths of the ligaments and the skin markers were updated. The rest lengths of the ligaments were determined with the leg in a straight position while taking into account the reference strains (Table A.1). The rest lengths of the rigid bone markers were set to zero.

Evaluation

To evaluate the solver's accuracy with varying marker numbers, several virtual rigid marker set combinations (visualized in Figure 4(B)) were imposed on every subject to guide the motion ranging from 3 to 7 markers.

As described in section 2.1, the soft tissue-integrated kinematic solver requires several input variables, including the ratio between different constraint types, i.e. ligament, contact and marker constraints. To evaluate the impact of this ratio, a grid search was conducted on a training set using the motion sequences from a subset of 5 randomly selected subjects ($\lambda_{marker/skin}$ and $\lambda_{contact}$.were varied between 0.01 and 1.2). The search evaluated the Root Mean Square Error (RMSE) on both tibiofemoral joint angles and translations, computed using the method of Grood and Suntay [36]. With the identified optimal constraint ratio, the solver's performance was evaluated on a test set consisting of the remaining 4 subjects in the four scanned positions.

Besides the constraint ratios, the soft tissue-integrated kinematic solver's performance also depends on accurate ligament properties, in particular the spring stiffness and the rest length. While literature offers various values, the reported range varies significantly across and within studies [37], [38]. To address this,

the possibility of and impact of an additional optimization step was explored on the same training and test set. In each frame, the bones were placed in their exact, known positions (ground truth). Utilizing the Nelder-Mead simplex algorithm, the stiffness of the ligaments were adjusted to minimize the amount of transformation (both translation and rotation) over all the frames for the training set of the five randomly selected subjects [39]. With the optimized ligament stiffnesses, we again evaluated the solver's performance on the test set (containing four subjects) in the four scanned positions.

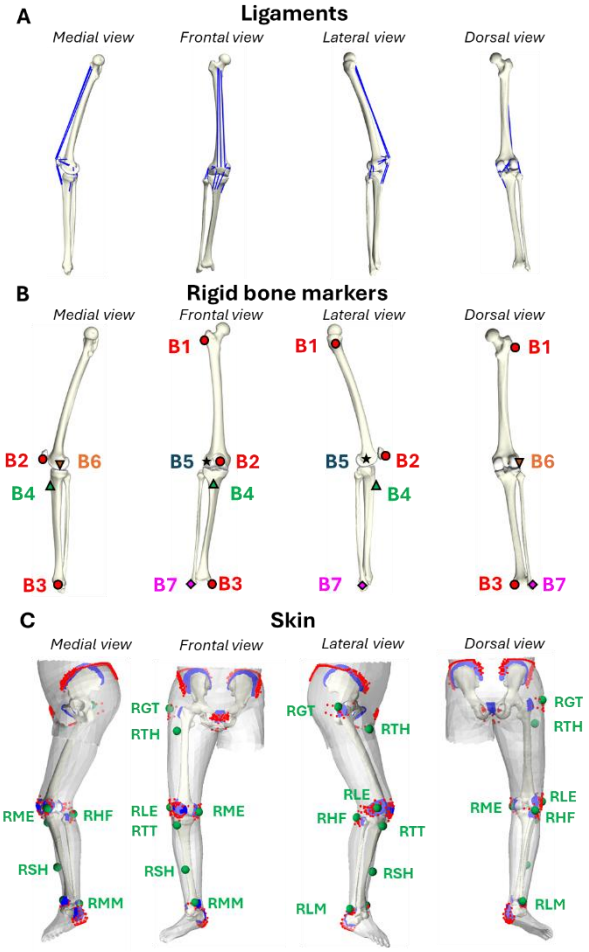

Figure 4: Medial, frontal, lateral and dorsal view of the knee model, indicating the ligaments and muscles(A), the rigid bone markers (B) and the skin with the skin markers (C). For the rigid bone markers (B), the initial set of 3 markers is shown in red with captions B1, B2 and B3. Extra markers were incrementally added, indicated with the captions B4 to B7. For the skin (C), the skin zones and

corresponding bone points used for guiding the motion are illustrated with respectively red and blue dots. Additionally, green markers and letters (R: Right, GT: Greater Trochanter, TH: Thigh, LE: Lateral Epicondyle, ME: Medial Epicondyle, HF: Head of Fibula, TT: Tibial Tuberosity, SH: Shank, LM: Lateral Malleolus, MM: Medial Malleolus) indicate the markers used for the inverse kinematic simulation with the revolute joint.

2.2.2. In-vitro validation experiment (B): Cadaveric Lower Limb mimicking squats in a CT scanner

The second validation experiment was designed to validate the soft tissue-integrated kinematic solver driven by solely skin information rather than rigid markers.

Input data and pre-processing

A cadaveric leg (male, 96 year, 1.60m and 50 kg) was scanned in four incremental flexion positions (15°, 49°, 78°, and 113° knee flexion) using a CT scanner (Siemens® SOMATOM Definition Flash, pixel size of 0.9766 mm x 0.9766 mm and slice thickness 0.6 mm). Further, the leg was instrumented with 16 needles in the subcutaneous fat (without affecting the range of motion) to allow for quantification of the skin motion. Following the scanning procedure, the femur, patella, tibia-fibula complex, and skin were again semi-automatically segmented and registered. Similar to Experiment A, a Principal Polynomial Shape Analysis (PPSA) model was generated using each registered structure (femur, patella, tibia-fibula complex, and skin) in the four original scan positions. Interpolation created a motion sequence with a 28 frames to computationally capture the movement. Simulated rigid bone marker and skin marker trajectories were generated by identifying corresponding indices on respectively the registered bony structures and registered skin surface, aligning with the bony landmarks. These indices were then used to extract the Euclidean coordinates of the corresponding points throughout the motion.

Anatomical and mechanical atlas

For the kinematic analysis, the same template model from Experiment A was employed (including the same soft constraints), as well as identical marker configurations were applied to the leg (visualized in Figure 4(B)). The rest lengths of the ligaments were determined with the leg in a straight position while taking into account the reference strains (Table A.1). Additionally, several skin regions (skin zones) were defined to evaluate the solver performance when driven by skin information as opposed to rigid markers (illustrated in Figure 4(C)). For the latter 2 additional segments were added, namely the pelvis and the talus-calcaneus complex. The rest lengths of the skin markers and the skin zones were determined in a straight position using reference strains of 0%. The rest length of the rigid bone markers were set to zero.

Evaluation

To evaluate the model's accuracy, we calculated the absolute error between the predicted and ground truth tibiofemoral joint angles and translations. Similar to the previous validation experiment, the joint angles and translations were computed using the method of Grood and Suntay in the scanned 4 positions [36].

The skin registration accuracy was evaluated using the position of needles as a reference (ground truth). For each needle, the skin points (identified by their indices) nearest to the needle's midpoint in the initial leg position were determined. Based on these indices, the anticipated locations of the needles in the second, third, and fourth leg position were predicted. The Euclidean distance between the expected position and the actual position of the needles relative to the registered skin in the first leg position was then a measure for the error of the registration.

Additionally, we conducted a comparative analysis of our solver against the conventional inverse kinematics with a revolute joint using both rigid bone markers and skin markers, as well as two computer vision methods, i.e. OSSO and SKEL.

For the conventional inverse kinematics with a revolute joint, a musculoskeletal model was created in AnyBody Modelling System (AMS) (v.8.0) (Anybody Technology A/S, Aalborg, Denmark). Three segments were defined (i.e. femur, tibia-fibula and patella). Inverse kinematic analysis determined the segment positions by minimizing the least-square difference between the simulated markers and the set of 7 rigid bone markers described in Figure 4 (B). Throughout the kinematic analysis, the tibia-fibula complex had six degrees of freedom relative to the global coordinate system. The tibiofemoral and patellofemoral joint were modelled as revolute joints. The outputted positions of the bones were exported. Subsequently, the joint angles and translations were calculated similar to described above and compared against the ground truth. The same procedure was repeated with skin markers typically used in traditional motion capture laboratory (Figure 4 (C), green markers).

Following, benchmarking with two recent computer vision methods was performed. OSSO and SKEL were installed on a Ubuntu 22.04 with 144 CPU cores and 376 GiB RAM. For OSSO, a pre-registered STAR mesh of the segmented skins surface served as input. OSSO first refits the pre-provided STAR mesh, then it repositions the skin mesh to a supine position for skeleton estimation. To match the posed skin mesh, it adjusts the position of the individual bones considering the distance to the posed skin mesh and a set of predefined joint limitations. To enable SKEL to process data, a SMPL mesh was first fitted to the segmented skin of the cadaver. SKEL then utilizes the fitted SMPL skin mesh as input and employs a regressor to re-rig the SMPL body model with a biomechanics skeleton. This process optimizes both joint locations and bone rotations for a more accurate representation. To enable a straightforward comparison between the joint angles calculated by OSSO and SKEL and those determined by other methods, the same coordinate system was used. To achieve this, the skeleton outputs of OSSO and SKEL were split into individual bony segments. The required landmarks to compute the joint angles were defined by landmark transfer using in-house available statistical shape models [35].

2.2.3. In-vitro validation experiment (C): Cadaveric Upper limb flexion-extension/pro-supination in a CT scanner

Input data and pre-processing

The final and third experiment was designed to assess the soft tissue-integrated kinematic solver capability for joints geometries different from the knee and therefor comprised the elbow joint. Hereto, a cadaver (female, 76 year, 1.70m and 52kg) was scanned in a CT scanner (Siemens® SOMATOM Definition Flash, pixel size of 0.8594 mm x 0.8594 mm and slice thickness 0.6 mm). The arm was scanned in 11 distinct positions, encompassing extension with pronation and supination as well as flexion at roughly 45, 90, and 135 degrees with the hand in neutral, fully pronated, and fully supinated positions. The humerus, ulna, radius and skin were manually segmented and non-rigidly registered [33]. Similar to the first two experiments, a Principal Polynomial Shape Analysis (PPSA) model was created based on the 11 scan positions encompassing each structure (humerus, ulna, radius, and skin). Subsequently and similar to the previous validation experiments, a high frequency motion sequence was interpolated (91 frame in this experiment) and rigid bone marker and skin marker trajectories were simulated.

Anatomical and mechanical atlas

A template model of the upper limb, consisting of humerus, ulna and radius, ligaments and contact conditions (details in Figure 5(A) and in Table A.2) was transferred to the available meshes. Again similar to the previous experiments, the rest lengths of the ligaments are determined in a specific joint position where the ligament length is equal to the ligament rest length or are determined by computing the rest length based on a known ligament strain in a certain joint position (Table A.2). The rest lengths of the skin markers are determined in the first frame of motion, which in the validation experiments corresponds to the leg/arm in the straight position. The rest length of the rigid bone markers were set to zero.

Evaluation

To evaluate the impact of increasing number of rigid markers, several combinations of rigid marker sets, were applied to each subject ranging from a minimal of 3 to 9 markers (depicted in Figure 5 (B)). Further, the accuracy in bony positions predictions was also evaluated using different skin markers sets (indicated with numbers 4, 7 and 10 in Figure 5 (C)) and dedicated skin regions. Subsequently, the humeroulnar and ulnoradial joint angles were determined following the ISB recommendations [40]. For the 11 scanned positions, the absolute error on the joint angles and translations were determined.

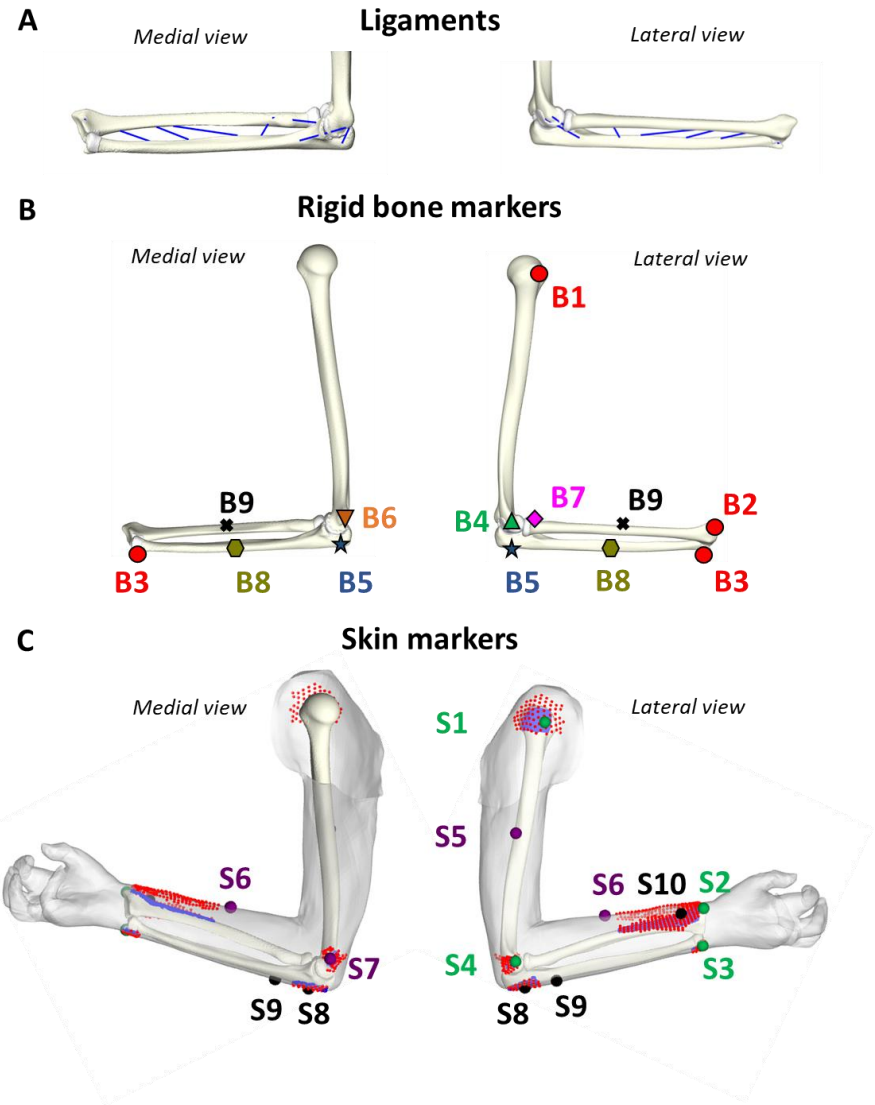

Figure 5: Medial and lateral views of the elbow model, highlighting the ligaments (A) and the placement of distinct markers: the rigid bone markers(B) and skin markers (C). (B) For the rigid bone markers, the initial set of 3 markers is indicated in red and captions B1, B2 and B3. Extra markers were incrementally added, indicated with the captions B4 to B9. (C) For the skin markers, sets of 4, 7 and 10 skin markers (S1-S4, S1-S7 and S1-S10) are illustrated in addition to the skin zones (red dots) and corresponding bone points (blue dots).

3. Results

3.1 In-vivo validation experiment (A): Healthy Lower Limb performing squats in a MRI scanner

This experiment had three main goals: to assess optimal ratios between constraint parameters, to validate the performance using rigid bone markers as input and to illustrate the impact of ligament property optimization.

The grid search on the training set of in-vivo knees data set identified optimal ratios between different constraint types ($\lambda_{ligament} = 1.0$, $\lambda_{contact} = 0.5$ and $\lambda_{marker/skin} = 1.0$). While this approach offers the possibility to further refine the performance of the soft tissue-integrated kinematic solver, the overall effect on the kinematic output, however, compared to a standard ratio of 1-1-1 in the current healthy subject population was marginal (<0.5° RMSE).

The optimized constraint ratios were then utilized in the kinematic solver throughout the in-vivo experiment on the test set. Figure 6 presents the absolute errors on the joint angles and translations. An overview of the median errors and error ranges is provided in table B.1. Generally, increasing the number of rigid bone markers led to a decrease in absolute errors for both joint angles and translations. Specifically, the median error for flexion-extension, ab-adduction and internal-external rotation decreased from 3.42°, 3.33° and 9.54° to 0.39°, 0.83° and 0.78°. Improvements were also observed in translation measurements.

570 Median errors for medio-lateral, anterior-posterior, and inferior-superior translation dropped from
571 9.98mm, 2.31mm, and 4.38mm to 2.74mm, 0.98mm, and 1.84mm, respectively.

572 The final goal of this experiment was to assess the impact of optimizing the ligament strengths. When
573 using the unoptimized ligament parameters obtained from literature, the error on the knee flexion is lower
574 than 1.5° in 18.75%, 37.50%, 68.75%, 100% and 100% of the frames for 3, 4, 5, 6 and 7 rigid bone markers.
575 Optimizing the ligament parameters resulted in ligament parameters that lie within the biomechanical
576 limits of human knees and a knee flexion error lower than 1.5° to 43.75%, 62.50%, 81.25%, 100% and
577 100% of the frames for 3, 4, 5, 6 and 7 rigid bone markers. Generally, optimizing ligament properties
578 reduced the absolute errors, with the exception of knee anterior-posterior translation and in the test case
579 of 5 rigid bone markers. Due to the limited amount of data, statistical significance testing was not
580 performed. The computation time for calculating the joint angles with unoptimized Matlab code without
581 parallel computing was about 17s per frame.

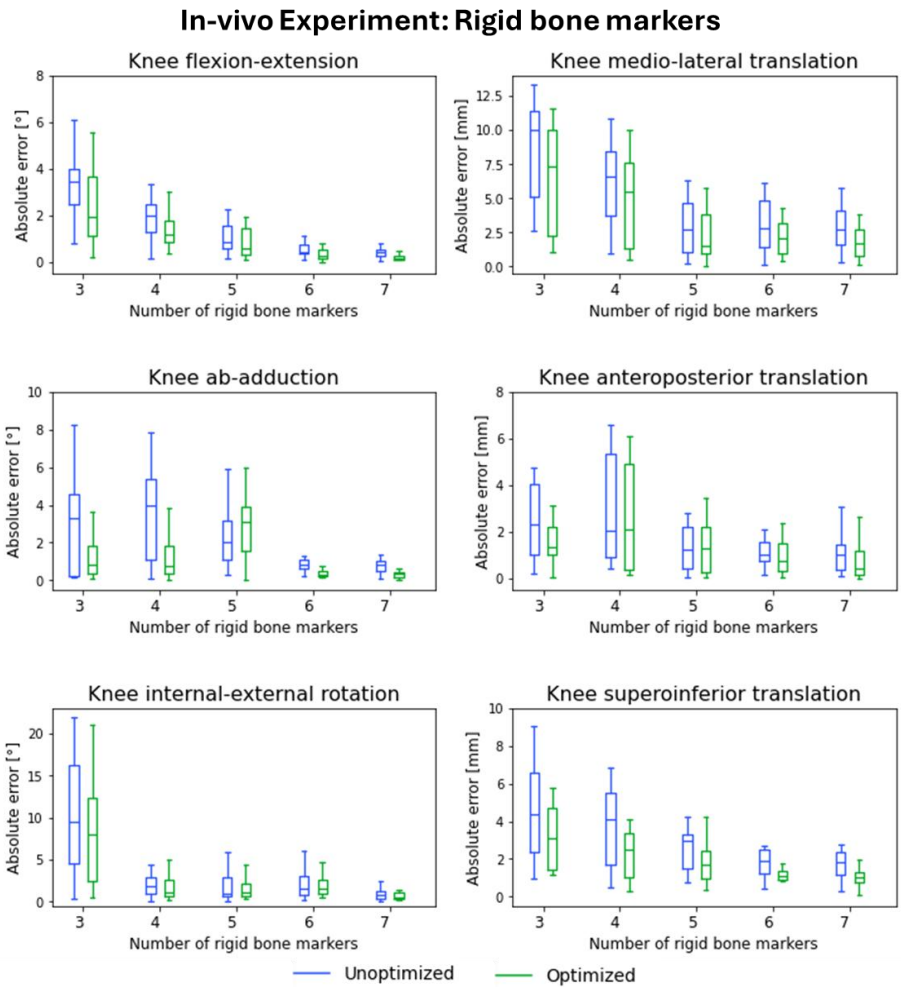

Figure 6: The absolute errors on the estimation of the flexion-extension, ab-adduction, internal-external rotation, medio-lateral translation, anteroposterior translation and superoinferior translation for the 4 acquired positions for different number of rigid bone markers using both unoptimized and optimized ligament parameters.

3.2 In-vitro validation experiment (B): Cadaveric Lower Limb performing squats in a CT scanner

This experiment evaluated the performance of the soft tissue-integrated kinematic solver utilizing different amounts of rigid bone markers as well as skin mesh information ('skin zones') to analyze knee kinematics during squat. Figures 7 and 8 depict the absolute errors for the rigid bone markers and skin zones, respectively. Table B.2 summarizes the median errors and error ranges across all configurations and

for the different kinematic solvers (i.e. soft tissue-integrated kinematic solver, traditional inverse kinematics using a revolute joint, OSSO and SKEL) used. Generally, increasing the number of rigid bone markers led to a decrease in absolute errors for both joint angles and translations. Specifically, the median error for flexion-extension, ab-adduction and internal-external rotation decreased from 5.38°, 13.89° and 9.34° to 0.59°, 0.74° and 1.48°. The revolute joint using rigid bone markers demonstrated a median knee flexion error of 2.72°. When using skin zones (illustrated in Figure 2(C)), rather than rigid bone markers, the median errors of the respective rotations slightly increased to respectively 0.85°, 3.00° and 3.08°. The skin surface based computer vision approaches, OSSO and SKEL, showed both higher rotation and translation errors than the soft tissue-integrated kinematic solver utilizing dedicated skin zones. Utilizing a marker protocol typically implemented in standard motion laboratories, the traditional inverse kinematics with a revolute joint showed a median knee flexion error of 7.29°.

The registration errors when fitting our template mesh to the skin in the different scan positions averaged at 16.5mm, 23.1mm, and 34.9mm for position 2, 3, and 4, respectively. The largest errors were found in the upper thigh region. Fitting STAR and SMPL to execute OSSO and SKEL yielded respectively mean errors of 28.1mm and 28.9mm for position 2, 30.8mm and 31.6mm for position 3, and 38.6mm and 40.1mm, for position 4.

The unoptimized Matlab code without parallel computing took on average 28 seconds per frame to position the 5 segments. After fitting STAR, OSSO required 177 seconds to reposition the skin to a lying down position, fit the skeleton in the lying pose, and then realign the skeleton (21 groups of bones) to match the adjusted skin. SKEL inferred the complete skeleton (24 bones with 46 degrees of freedom) in on average 103 seconds per frame after fitting SMPL. The traditional inverse kinematics approach implemented in the AMS solved the femur, tibia, and patellar position in on average 0.05 seconds per frame.

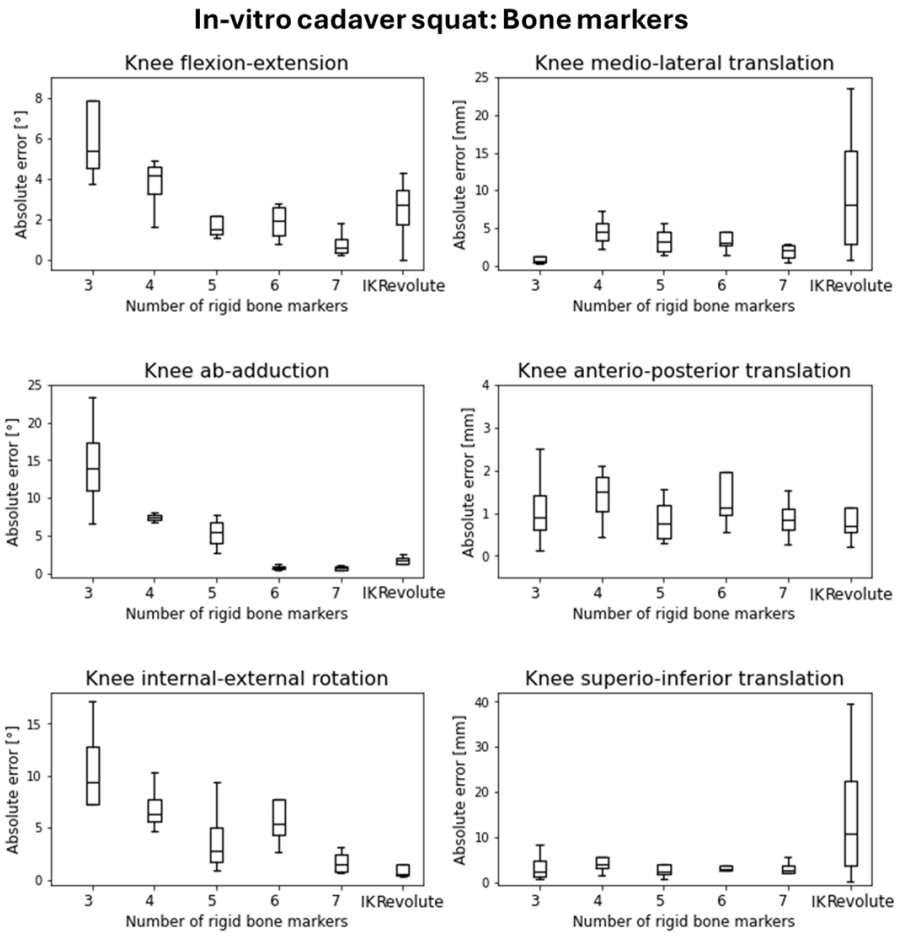

615

616 *Figure 7: The absolute errors in estimating the flexion-extension, abduction-adduction, internal-external*
617 *rotation, medio-lateral translation, anteroposterior translation, and superoinferior translation of the*
618 *tibiofemoral joint for the 4 acquired positions for varying number of rigid bone markers. This includes*
619 *assessments using unoptimized ligament parameters in the soft tissue -integrated kinematic solver, as well*
620 *as the absolute error using the traditional Inverse Kinematics (IK) with a revolute joint.*

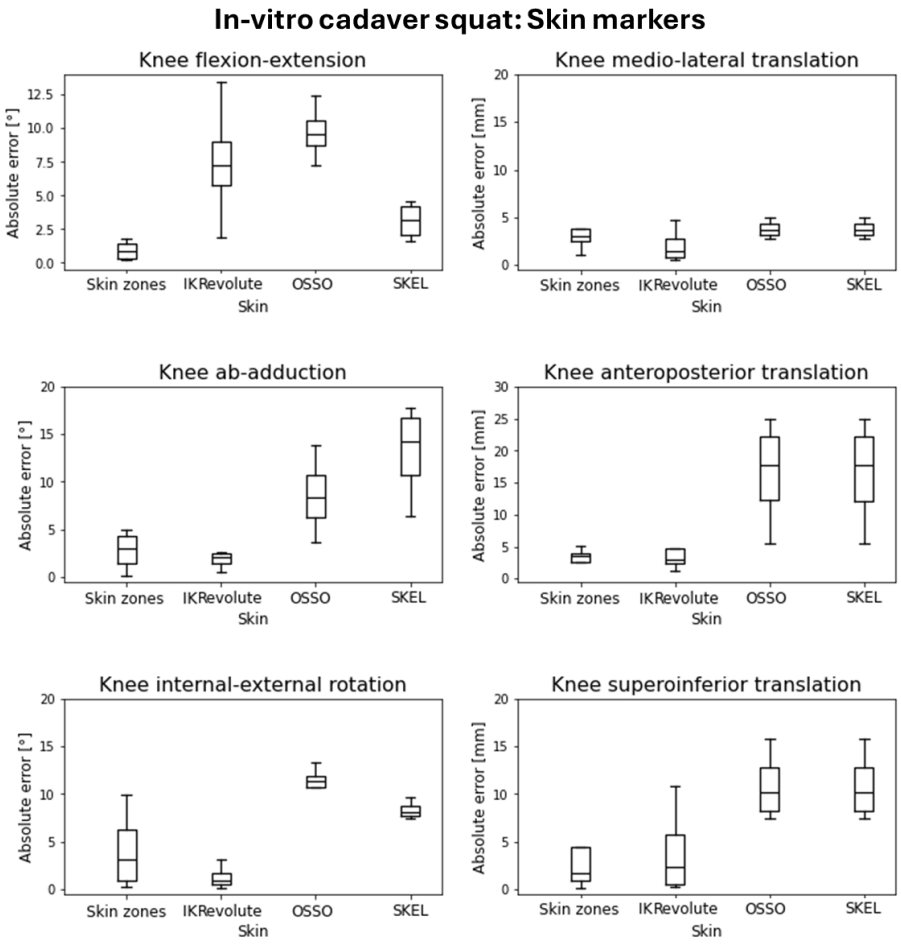

Figure 8: The absolute errors in estimating the flexion-extension, abduction-adduction, internal-external rotation, medio-lateral translation, anteroposterior translation, and superoinferior translation of the tibiofemoral joint for the 4 acquired positions. This includes the absolute error using unoptimized ligament parameters in the soft tissue -integrated kinematic solver using skin zones as input, as well as when using the traditional Inverse Kinematics (IK) with a revolute joint and two computer vision methods: OSSO and SKEL.

3.3 In-vitro validation experiment (C): Cadaveric Upper limb flexion-extension/pro-supination in a CT scanner

The final validation experiment aimed to assess the solver's performance on a joint beyond the knee, specifically focusing on a complex coupled joint, namely the elbow joint. The performance was evaluated

under various configurations involving different amounts of rigid bone markers, varying number of skin markers and skin zones. A visual representation of the absolute errors can be found in Figure 9, while a detailed overview can be found in table B.3. The optimized ratios between different constraint types were kept the same as in the earlier described in-vivo experiment. With six or more rigid bone markers, the soft tissue-integrated kinematic solver's error in solving the 18-degree-of-freedom system reaches a plateau. The median error for the two dominant joint angles stabilizes starting from 6 rigid bone markers, ranging between 1.09 and 1.44 degrees for humeroulnar flexion and between 0.84 and 1.13 degrees for ulnoradial pronation-supination. Similar trends were observed for non-dominant movement patterns with the median absolute error on the humeroulnar axial rotation ranging between 0.24 and 0.38 degrees and the error on the orientation of the pro-supination axis between 1.43 and 1.59 degrees. Incorporating skin zones instead of rigid bone markers increased the median error largely. Using skin zones resulted in a median error increase to 3.80 degrees for humeroulnar flexion-extension and 2.94 degrees for ulnoradial pronation-supination. A movie of the validation experiment with skin zones, including both ground truth and predicted bony positions can be found in Video 1. For this 18-degree-of-freedom system with unoptimized Matlab code and no parallel processing, calculating the joint angles and translations took per frame on average 6.4 seconds with 9 rigid bone markers and 4.5 seconds when driven by the skin zones.

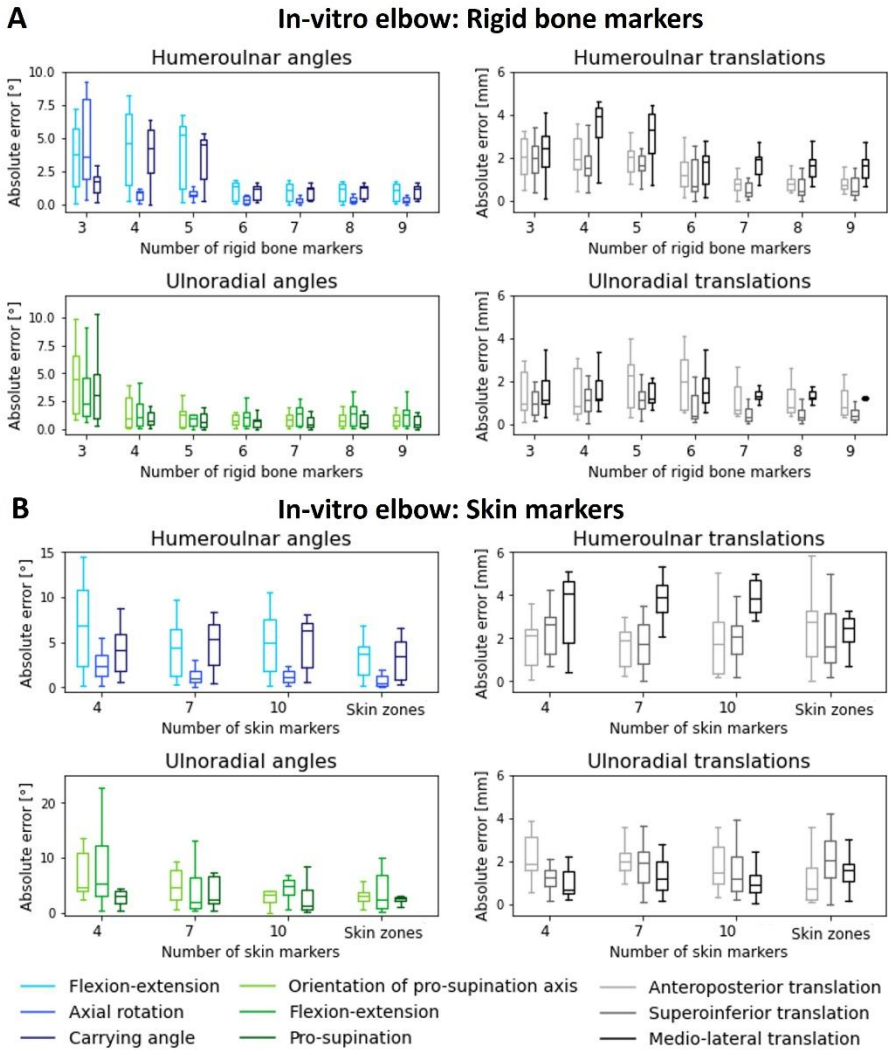

649

650 *Figure 9: The absolute errors on the estimation of the humeroulnar and ulnoradial angles and translations*

651 *for the 11 acquired positions for different sets of rigid bone markers (A) and skin markers (B).*

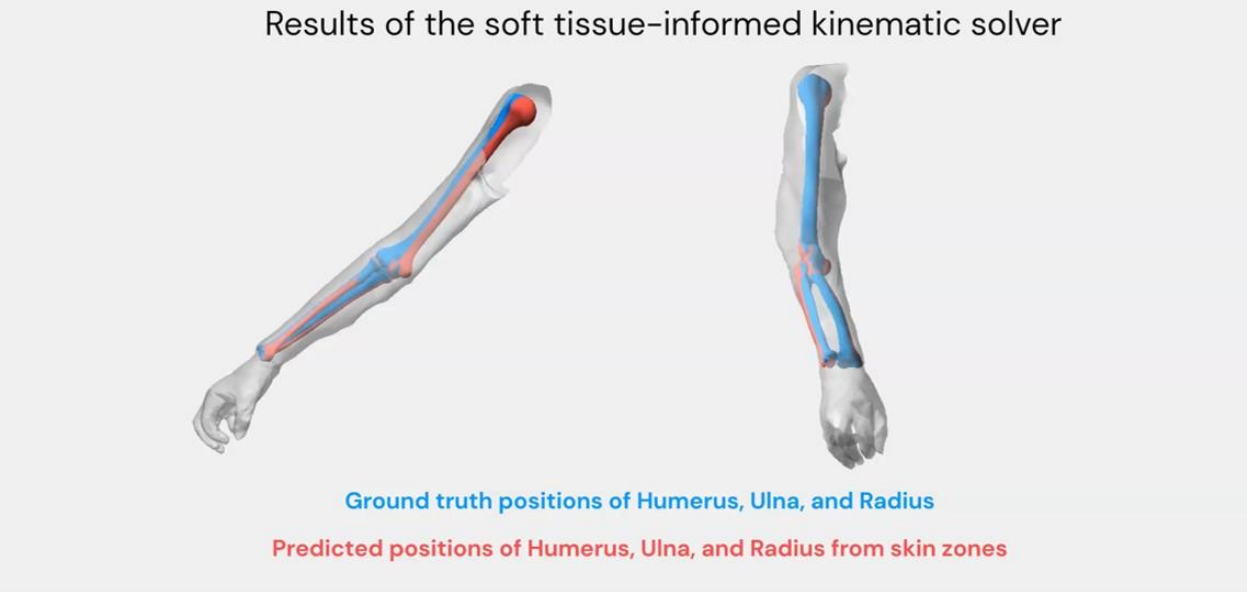

*Video 1: In the movie, the skin is illustrated in grey and the ground truth bony positions are shown in blue. The predicted positions of the humerus, ulna and, radius are indicated in red. (*https://doi.org/10.5281/zenodo.11350837.)

4. Discussion

This paper presents a soft tissue-integrated kinematic solver that operates on segment definitions rather than joint definitions and incorporates soft tissue structures such as ligaments, cartilage and muscles. The input of this soft tissue-integrated kinematic solver expands beyond bone markers and reflective skin markers. It can also directly analyze the skeletal motion from skin surfaces meshes, using designated skin zones that contribute to determining the underlying bone positions. The proposed methodology demonstrated good agreement with the ground truth in three experiments (one in-vivo and two in-vitro experiments). Compared to current state-of-the-art methods (i.e. inverse kinematics with a revolute joint and computer vision approached (OSSO and SKEL)), our method delivers almost without exception equal or improved results.

4.1 Rigid bone marker validation

Both the in-vitro and in-vivo experiments employed rigid bone markers to solve the position of three bones for a total of 18 degrees of freedom. Using three rigid bone markers, the soft tissue-integrated kinematic solver solves an underdetermined system. Nevertheless, the error on the main movement (flexion-extension in the knee and humeroulnar joint) remains reasonable with errors lower than 7.5 degrees. As expected, incorporating more markers consistently reduces errors in joint angles and translations. For example, adding a fifth rigid bone marker in the in-vivo experiment largely reduces the error on the mediolateral translation. The fifth rigid bone marker was placed at the lateral epicondyle, which plays an important role in tracking this specific outcome parameter. Interestingly, further increasing the number of markers yield marginal additional improvement in accuracy. The latter shows the potential of the soft tissue-integrated kinematic solver, to robustly solve 6 DOF of both tibia and femur with only 4 rigid bone markers attached to these structures. Similarly, in the in-vitro cadaver elbow experiment the ulnoradial and humeroulnar joint angles did not improve extensively after adding respectively the 5^{th} and 6^{th} rigid

bone marker to solve the 18 DOF system. In the in-vitro cadaver leg experiment, the soft tissue-integrated kinematic solver was assessed next to the traditional inverse kinematics approach with a revolute joint. When sufficient (more than 4) rigid bone markers were used, the proposed kinematic solver performed similar or even better than the revolute joint for the main motion (i.e. tibiofemoral flexion). The implemented revolute joints used a fixed axis, which resulted in higher errors in the deep flexion than would a floating axis revolute joint have been implemented. The low error in the revolute joint's abduction, adduction, and internal/external rotation measurements reflects the limited range of these rotations during the studied squatting motion. Unlike the soft tissue-integrated kinematic solver that considers all possible movements, a revolute joint inherently restricts these rotations.

4.2 Skin marker/skin zones validation

Compared to rigid bone markers, both skin markers and complete skin analysis produce higher errors. This can be attributed to the inherent noise present in skin movement data, which is absent in the rigid bone marker data. Unlike rigid bone markers that are directly attached to the underlying skeletal structure, skin is subject to movement artifacts arising from soft tissue deformation, muscle contractions, and skin slippage relative to the bone. These factors introduce variability and noise into the skin motion data that are not present in the direct, rigid tracking of bone markers. The soft tissue-integrated kinematic solver outperforms the revolute joint in tibiofemoral flexion. The proposed kinematic solver considers data from several skin regions, providing a more comprehensive view of the movement compared to the traditional method (i.e. using reflective markers on the skin in combination inverse kinematics with a revolute joint) which relies on data of individual points. Again, similar to the rigid bone markers, the revolute joint's fixed axis hampers the accuracy in deep flexion. Further, the soft tissue-integrated kinematic solver demonstrated a closer agreement with ground truth data for biomechanical applications compared to existing computer vision methods (OSSO and SKEL). While SKEL surpasses OSSO in capturing knee flexion, their performance is comparable for other degrees of freedom. This likely stems from SKEL's skeletal

model, which represents the knee as a single degree of freedom joint with coupled rotations and translations, based on the joint kinematic parameterizations [41], [42]. In contrast, OSSO utilizes a ball-and-socket joint combined with a simplified representation of the knee ligaments.

4.3 Comparison with State-of-the-Art Methods

Beyond traditional marker-based systems and 4D scanners/mesh based systems, various markerless technologies exist. Examples include vision-based systems (e.g. Theia Markerless) and sensor-based systems (e.g. Inertial Measurement Units (IMUs)). Theia, leverages on deep learning to infer 3D skeletal pose from synchronized video cameras. Kanko et al. compared Theia's accuracy to a marker-based system for tibiofemoral kinematics during running. Their study, using 8 cameras and analyzing two running sequences from 21 participants, reported root-mean square errors of 4.2°, 7.2°, and 9.4° for flexion-extension, abduction-adduction, and internal-external rotation, respectively [43]. Likewise, the sensor-based systems have been evaluated. Antules et al. found a mean absolute error of 2.6 degrees on knee flexion when performing a standing knee bend [44]. Cordillet et al. on the other hand found that the knee flexion error stays below 3.8° while the mean knee internal/external rotation and knee ab-adduction error was respectively 6.65° and 5.92° during a pedaling motion [45]. Lastly, Mihcin et al. reported a maximum RMSE of 5.9° for in vivo knee flexion motion during activities of daily living when comparing IMUs and a marker-based system [46]. It is important to note that the vision- and sensor-based systems were evaluated against marker-based ground truth data, whereas our kinematic solver is compared to MRI data. Despite this difference in comparison standards, these results suggest that the introduced soft-tissue - integrated kinematic solver, using skin regions, provides an improved accuracy.

On the other hand, in traditional biomechanics, numerous efforts have been undertaken to improve on the traditional kinematic solvers. An example is Force Dependent Kinematics (FDK) [12]. FDK starts with an initial estimate of the primary movement. This estimate is then used in a process called ‘Inverse

Dynamics' to concurrently estimate the muscle, ligament and joint contact forces with the secondary kinematics. Dejtiar et al. (2020) implemented this method for the tibiofemoral and patellofemoral joint. Their in-vivo validation study using skin markers reported a mean error of -2.08° ± 0.10° for abduction-adduction and 1.77° ± 0.86° for internal-external rotation, which is lower than the errors obtained with the soft tissue-integrated kinematic solver. Implementing this method for the in-vitro cadaver experiment was not possible as we did not have exact reaction forces at the feet. Further, Dejtiar et al. tested 4 healthy individuals and therefore included active muscle forces. In this study a cadaveric leg was used. Consequently, there were no active muscle contributions. The FDK methodology intrinsically balances muscle, soft tissue, and joint reaction forces while optimizing secondary kinematics. Consequently, omitting muscles from the model disrupts this balancing mechanism. While FDK leverages kinematic analysis with revolute joint as a starting point, the proposed solver offers more precise input data. This opens doors for future studies to combine the strengths of both methods, potentially leading to faster and more accurate results.

4.4 Performance sensitivity and computation time

The findings and solver performance for all systems highly depend on the quality and extent of input data driving the solvers. Three particular issues, namely skin registration, the definition and number of segments and their respective soft tissue properties are of high importance and impact on the accuracy and the computational efficiency for all systems in a varying degree.

A first critical consideration is skin registration when utilizing individual skin zones as input. Accurate registration of soft tissue remains a challenge. The STAR and SMPL fitting exhibit larger registration errors. This is likely due to the use of a limited number of model components (blend shapes). These blend shapes did not capture the full complexity of human skin, leading to discrepancies between the model and real anatomy. The registration errors impact the downstream results. For instance, the OSSO approach utilizes

"skin to skeleton pairs," where a single skin vertex is linked to a single skeletal vertex. In our approach, similarly skin-bone correspondence is defined to guide the motion. Consequently, registration inaccuracies can heavily influence the final outcome.

Further, in biomechanical research, the vast differences in the reported soft tissue strength parameters across the literature presents a challenge [37], [38]. To counter this, we optimized the ligament parameters specifically for the in-vivo dataset. This optimization kept the ligament parameters within the physiological range and generally reduced errors, with the exception of knee anterior-posterior translation and in the test case of 5 rigid bone markers. This finding suggests that either more detailed information or a closer examination of specific ligament parameters is necessary for this soft tissue-integrated kinematic solver.

Comparing the computational efficiency across the different methods is challenging due to the variations in the skeleton complexity (i.e. full skeleton represented with 21 segments and 24 segments in respectively OSSO and SKEL versus limited amount of segments in the soft tissue-integrated kinematic solver and when employing the revolute joint). Our method exhibits similar computation times to SKEL and OSSO. However, it is important to acknowledge that our method is under development, and further optimization is anticipated. Despite this, our approach demonstrates improved biomechanical output by incorporating soft tissue structures while maintaining comparable computational efficiency to existing methods.

4.5 Strengths

The presented soft tissue-integrated kinematic solver offers several key strengths that address limitations inherent in conventional biomechanical methods. Unlike traditional approaches that often rely on simplified, hard joint constraints, our solver operates directly on segment definitions and explicitly incorporates the influence of relevant soft tissue structures (i.e., ligaments, tendons, cartilage contact, fascia regions) modeled as springs between the segment and its neighboring segments and/or skin. This core mechanism enables the exploration of a more complete spectrum of human movement,

encompassing all degrees of freedom while guiding the motion in a biologically meaningful way. This physiological constraint-based approach acts as a regulator, effectively preventing the calculation of unreasonable or physically implausible joint angles, a common issue with inverse kinematics and overly simplified joint definitions [47], [48]. Consequently, this inherent stability and physiological grounding lead to more realistic and reliable simulations of human movement across a wide range of activities and joints.

4.5 Limitations and future work

While this study offers valuable insights into the potential of the soft tissue-integrated kinematic solver, it is important to acknowledge some inherent limitations in the validation. While the study explores both in-vitro and in-vivo settings, only one experiment utilized real-world data (in-vivo). Future work includes testing subjects in both traditional and non-traditional Activities of Daily Living, and more challenging sport motions [49], [50]. Further, the amount of subjects within each experiment was limited. This restricts the ability to draw statistically significant conclusions regarding the performance of different marker setups or comparisons between experiments. Moreover, the in-vivo data collection focused on a side-lying position. Additionally, for the skin marker experiments, we virtually generated skin marker trajectories. While these trajectories incorporate a certain degree of skin motion error due to the imperfect registration of the skin meshes, they do not fully replicate the soft tissue artifacts observed in real skin marker trajectories. Future research involves testing the methodology with actual skin markers.

To fully implement the current methodology, knowledge of the subject's bony anatomy is essential. To address this limitation, future research will focus on developing a method to infer the underlying skeleton from skin surface data using 3D input data from either MRI or CT. In contrast to OSSO and SKEL, which utilize bone groups resulting in less than 25 segments for the entire skeleton, our approach will ensure a higher level of anatomical detail by working with individually and non-rigidly registered bones. When utilizing skin marker data, individual anatomical information will still be necessary. Consequently, future

work includes exploring a similar approach to Di Pietro et al. to scale a standardized skeletal model using the inferred markers [51].

5. Conclusion

This paper introduced a soft tissue-integrated kinematic solver. Unlike conventional biomechanical methods relying on hard joint constraints, this solver operates on segment definitions and incorporates relevant soft tissue structures. This enables the exploration of all degrees of freedom while maintaining computational efficiency. Furthermore, the solver facilitates the analysis of both marker and skin data. Future work includes verifying the soft tissue-integrated kinematic solver using full body 4D scans as input.

Funding sources

This work was supported by two Aspirant Grants from the Research Foundation-Flanders (#1137723N, #1122821N, FWO) and by a Senior Clinical Investigator Fellowship Grant from the Research Foundation-Flanders (#1842619N, FWO).

Conflict of interest statement

The authors declare no competing interests.

Author Contribution

All authors have made substantial contributions to all of the following: (1) the conception and design of the study, or acquisition of data, or analysis and interpretation of data, (2) drafting the article or revising it critically for important intellectual content, (3) final approval of the version to be submitted.

References

[1] S. L. Colyer, M. Evans, D. P. Cosker, and A. I. T. Salo, “A Review of the Evolution of Vision-Based Motion Analysis and the Integration of Advanced Computer Vision Methods Towards Developing a Markerless System,” Dec. 01, 2018, *Springer*. doi: 10.1186/s40798-018-0139-y.

[2] M. S. Andersen, “Introduction to musculoskeletal modelling,” in *Computational Modelling of Biomechanics and Biotribology in the Musculoskeletal System: Biomaterials and Tissues*, Elsevier, 2020, pp. 41–80. doi: 10.1016/B978-0-12-819531-4.00004-3.

[3] T.-W. Lu, D. Phil, T.-W. Lu, and J. J. O’connor, “Bone position estimation from skin marker co-ordinates using global optimisation with joint constraints,” 1999.

[4] S. L. Delp *et al.*, “OpenSim: Open-source software to create and analyze dynamic simulations of movement,” *IEEE Trans Biomed Eng*, vol. 54, no. 11, pp. 1940–1950, Nov. 2007, doi: 10.1109/TBME.2007.901024.

[5] J. Rasmussen, “The anybody modeling system,” in *DHM and Posturography*, Elsevier, 2019, pp. 85–96. doi: 10.1016/B978-0-12-816713-7.00008-8.

[6] J. and R. D. K. and B. D. L. Andersen M. S. and Rasmussen, “Validation of Knee Joint Models – An In Vivo Study,” in *6th World Congress of Biomechanics (WCB 2010). August 1-6, 2010 Singapore*, J. C. H. Lim C. T. and Goh, Ed., Berlin, Heidelberg: Springer Berlin Heidelberg, 2010, pp. 1288–1291.

[7] B. K. Lahkar *et al.*, “Development and evaluation of a new methodology for Soft Tissue Artifact compensation in the lower limb,” *J Biomech*, vol. 122, Jun. 2021, doi: 10.1016/j.jbiomech.2021.110464.

[8] A. Humphries, S. Cirovic, and A. F. Shaheen, “Shoulder Bone Geometry Affects the Active and Passive Axial Rotational Range of the Glenohumeral Joint,” *American Journal of Sports Medicine*, vol. 45, no. 13, pp. 3010–3019, Nov. 2017, doi: 10.1177/0363546517716926.

[9] A. R. Karduna, G. R. Williams, J. L. Williams, and J. P. Iannotti, “Kinematics of the glenohumeral joint: influences of muscle forces, ligamentous constraints and articular geometry,” *Orthopaedic Research Society*, vol. 14, pp. 986–993, 1996.

[10] L. Blankevoort, R. Huiskes, and A. De Lange, “The envelope of passive knee joint motion,” vol. 21, no. 9, pp. 705–720, 1988.

[11] M. S. Andersen, J. Rasmussen, D. K. Ramsey, and D. L. Benoit, “Validation of Knee Joint Models-An In Vivo Study,” vol. 31, pp. 1288–1291, 2010, [Online]. Available: www.springerlink.com

[12] M. S. Andersen, M. De Zee, M. Damsgaard, D. Nolte, and J. Rasmussen, “Introduction to force-dependent kinematics: Theory and application to mandible modeling,” *J Biomech Eng*, vol. 139, no. 9, Sep. 2017, doi: 10.1115/1.4037100.

[13] D. L. Dejtiar, C. M. Dzialo, P. H. Pedersen, K. K. Jensen, M. K. Fleron, and M. S. Andersen, “Development and evaluation of a subject-specific lower limb model with an eleven-degrees-of-freedom natural knee model using magnetic resonance and biplanar x-ray imaging during a quasi-static lunge,” *J Biomech Eng*, vol. 142, no. 6, Jun. 2020, doi: 10.1115/1.4044245.

[14] M. Marieswaran, A. Sikidar, A. Goel, D. Joshi, and D. Kalyanasundaram, “An extended OpenSim knee model for analysis of strains of connective tissues,” *Biomed Eng Online*, vol. 17, no. 1, Apr. 2018, doi: 10.1186/s12938-018-0474-8.

[15] H. Xu, D. Bloswick, and A. Merryweather, “An improved OpenSim gait model with multiple degrees of freedom knee joint and knee ligaments,” *Comput Methods Biomech Biomed Engin*, vol. 18, no. 11, pp. 1217–1224, Aug. 2015, doi: 10.1080/10255842.2014.889689.

[16] A. Schmitz and D. Piovesan, “Development of an Open-Source, Discrete Element Knee Model,” *IEEE Trans Biomed Eng*, vol. 63, no. 10, pp. 2056–2067, Oct. 2016, doi: 10.1109/TBME.2016.2585926.

[17] A. Ancillao, E. Aertbeliën, and J. De Schutter, “Effect of the soft tissue artifact on marker measurements and on the calculation of the helical axis of the knee during a gait cycle: A study on the CAMS-Knee data set,” *Hum Mov Sci*, vol. 80, Dec. 2021, doi: 10.1016/j.humov.2021.102866.

[18] B. M. Potvin, M. S. Shourijeh, K. B. Smale, and D. L. Benoit, “A practical solution to reduce soft tissue artifact error at the knee using adaptive kinematic constraints,” *J Biomech*, vol. 62, pp. 124–131, Sep. 2017, doi: 10.1016/j.jbiomech.2017.02.006.

[19] V. Bonnet *et al.*, “A constrained extended Kalman filter for the optimal estimate of kinematics and kinetics of a sagittal symmetric exercise,” *J Biomech*, vol. 62, pp. 140–147, Sep. 2017, doi: 10.1016/j.jbiomech.2016.12.027.

[20] A. K. Einfeldt, L. Budde, A. Ortigas-Vásquez, A. Sauer, M. Utz, and E. Jakubowitz, “A new method called MiKneeSoTA to minimize knee soft-tissue artifacts in kinematic analysis,” *Sci Rep*, vol. 14, no. 1, Dec. 2024, doi: 10.1038/s41598-024-71409-z.

[21] V. Bonnet, V. Richard, V. Camomilla, G. Venture, A. Cappozzo, and R. Dumas, “Joint kinematics estimation using a multi-body kinematics optimisation and an extended Kalman filter, and embedding a soft tissue artefact model,” *J Biomech*, vol. 62, pp. 148–155, Sep. 2017, doi: 10.1016/j.jbiomech.2017.04.033.

[22] M. Begon, C. Bélaise, A. Naaim, A. Lundberg, and L. Chèze, “Multibody kinematics optimization with marker projection improves the accuracy of the humerus rotational kinematics,” *J Biomech*, vol. 62, pp. 117–123, Sep. 2017, doi: 10.1016/j.jbiomech.2016.09.046.

[23] V. Camomilla, R. Dumas, and A. Cappozzo, “Human movement analysis: The soft tissue artefact issue,” Sep. 06, 2017, *Elsevier Ltd*. doi: 10.1016/j.jbiomech.2017.09.001.

[24] S. Mihcin, “Methodology on Co-Registration of Mri and Optoelectronic Motion Capture Marker Sets: In-Vivo Wrist Case Study,” *Hittite Journal of Science & Engineering*, vol. 6, no. 2, pp. 99–107, 2019, doi: 10.17350/HJSE19030000134.

[25] M. Loper, N. Mahmood, J. Romero, G. Pons-Moll, and M. J. Black, “SMPL: A Skinned Multi-Person Linear Model,” *ACM Trans Graph*, vol. 34, no. 6, p. 248, 2015, doi: 10.1145/2816795.2818013.

[26] N. Mahmood, N. Ghorbani, N. F. Troje, G. Pons-Moll, and M. J. Black, “AMASS: Archive of Motion Capture as Surface Shapes,” in *2019 IEEE/CVF International Conference on Computer Vision*, 2019, pp. 5441–5450. doi: 10.1109/ICCV.2019.00554.

[27] G. Pons-Moll, J. Romero, N. Mahmood, and M. J. Black, “Dyna: A Model of Dynamic Human Shape in Motion,” *ACM Trans Graph*, vol. 36, no. 4, p. 54, 2017, doi: 10.1145/3072959.3073685.

[28] M. Keller, S. Zuffi, M. J. Black, and S. Pujades, “OSSO: Obtaining Skeletal Shape from Outside,” in *2022 IEEE/CVF Conference on Computer Vision and Pattern Recognition (CVPR)*, 2022, pp. 20460–20469. doi: 10.1109/CVPR52688.2022.01984.

[29] M. Keller *et al.*, “From Skin to Skeleton: Towards Biomechanically Accurate 3D Digital Humans,” *ACM Trans Graph*, vol. 42, no. 6, Dec. 2023, doi: 10.1145/3618381.

[30] C. S. Shin, A. M. Chaudhari, and T. P. Andriacchi, “The influence of deceleration forces on ACL strain during single-leg landing: A simulation study,” *J Biomech*, vol. 40, no. 5, pp. 1145–1152, 2007, doi: 10.1016/j.jbiomech.2006.05.004.

[31] D. L. , Butler, M. D. , Kay, and D. C. Stouffer, “Comparison of material properties in fascicle-bone units from human patellar tendon and knee ligaments,” *J Biomech*, vol. 19, no. 6, pp. 425–432, 1986.

[32] A. Van Oevelen *et al.*, “The relation between meniscal dynamics and tibiofemoral kinematics,” *Sci Rep*, vol. 14, no. 1, Dec. 2024, doi: 10.1038/s41598-024-59265-3.

[33] E. A. Audenaert *et al.*, “Cascaded statistical shape model based segmentation of the full lower limb in CT,” *Comput Methods Biomech Biomed Engin*, vol. 22, no. 6, pp. 644–657, Apr. 2019, doi: 10.1080/10255842.2019.1577828.

[34] K. Duquesne, N. Nauwelaers, P. Claes, and E. A. Audenaert, “Principal polynomial shape analysis: A non-linear tool for statistical shape modeling,” *Comput Methods Programs Biomed*, vol. 220, Jun. 2022, doi: 10.1016/j.cmpb.2022.106812.

[35] E. A. Audenaert, C. Pattyn, G. Steenackers, J. De Roeck, D. Vandermeulen, and P. Claes, “Statistical Shape Modeling of Skeletal Anatomy for Sex Discrimination: Their Training Size, Sexual Dimorphism, and Asymmetry,” *Front Bioeng Biotechnol*, vol. 7, Nov. 2019, doi: 10.3389/fbioe.2019.00302.

[36] E. S. Grood and W. J. Suntay, “A Joint Coordinate System for the Clinical Description of Three-Dimensional Motions: Application to the Knee,” *J Biomech Eng*, vol. 105, no. 2, pp. 136–144, 1983, doi: 10.1115/1.3138397.

[37] H. J. Cho and D. S. Kwak, “Mechanical properties and characteristics of the anterolateral and collateral ligaments of the knee,” *Applied Sciences (Switzerland)*, vol. 10, no. 18, Sep. 2020, doi: 10.3390/APP10186266.

[38] A. E. Peters, B. Geraghty, K. T. Bates, R. Akhtar, R. Readioff, and E. Comerford, “Ligament mechanics of ageing and osteoarthritic human knees,” *Front Bioeng Biotechnol*, vol. 10, Aug. 2022, doi: 10.3389/fbioe.2022.954837.

[39] J. C. Lagarias, J. A. Reeds, M. H. Wright, and P. E. Wright, “Convergence Properties of the Nelder–Mead Simplex Method in Low Dimensions,” *SIAM Journal on Optimization*, vol. 9, no. 1, pp. 112–147, 1998, doi: 10.1137/S1052623496303470.

[40] G. Wu *et al.*, “ISB recommendation on definitions of joint coordinate systems of various joints for the reporting of human joint motion - Part II: Shoulder, elbow, wrist and hand,” *J Biomech*, vol. 38, no. 5, pp. 981–992, May 2005, doi: 10.1016/j.jbiomech.2004.05.042.

[41] P. S. Walker, J. S. Rovick, and D. D. Robertson, “The Effects Of Kee Brace Hinge Design And Placement On Joint Mechanics,” 1988.

[42] A. Rajagopal, C. L. Dembia, M. S. DeMers, D. D. Delp, J. L. Hicks, and S. L. Delp, “Full-Body Musculoskeletal Model for Muscle-Driven Simulation of Human Gait,” *IEEE Trans Biomed Eng*, vol. 63, no. 10, pp. 2068–2079, Oct. 2016, doi: 10.1109/TBME.2016.2586891.

[43] R. M. Kanko, J. B. Outerleys, E. K. Laende, W. S. Selbie, and K. J. Deluzio, “Comparison of Concurrent and Asynchronous Running Kinematics and Kinetics From Marker-Based and Markerless Motion Capture Under Varying Clothing Conditions,” *J Appl Biomech*, vol. 40, no. 2, pp. 129–137, 2024, doi: 10.1123/jab.2023-0069.

[44] R. Antunes, P. Jacob, A. Meyer, M. A. Conditt, M. W. Roche, and M. A. Verstraete, “Accuracy of measuring knee flexion after tka through wearable imu sensors,” *J Funct Morphol Kinesiol*, vol. 6, no. 3, Sep. 2021, doi: 10.3390/jfmk6030060.

[45] S. Cordillet, N. Bideau, B. Bideau, and G. Nicolas, “Estimation of 3D knee joint angles during cycling using inertial sensors: Accuracy of a novel sensor-to-segment calibration procedure based on pedaling motion,” *Sensors (Switzerland)*, vol. 19, no. 11, Jun. 2019, doi: 10.3390/s19112474.

[46] S. Mihcin, “Simultaneous Validation of Wearable Motion Capture System for Lower Body Applications: Over Single Plane Range of Motion (RoM) and Gait Activities,” *Biomedical Engineering* , vol. 67, no. 3, pp. 185–199, 2022.

[47] A. Aristidou and J. Lasenby, “Inverse Kinematics: a review of existing techniques and introduction of a new fast iterative solver,” 2009.

[48] Z. Benhmidouch, S. Moufid, and A. A. Omar, “A comparative study of human inverse kinematics techniques for lower limbs,” Feb. 2023, [Online]. Available: http://arxiv.org/abs/2302.10769

[49] X. Chen, A. Pang, W. Yang, Y. Ma, L. Xu, and J. Yu, “SportsCap: Monocular 3D Human Motion Capture and Fine-Grained Understanding in Challenging Sports Videos,” *Int J Comput Vis*, vol. 129, no. 10, pp. 2846–2864, Oct. 2021, doi: 10.1007/s11263-021-01486-4.

[50] S. Mihcin *et al.*, “Database covering the prayer movements which were not available previously,” *Sci Data*, vol. 10, no. 1, Dec. 2023, doi: 10.1038/s41597-023-02196-x.

[51] A. Di Pietro, A. Bersani, C. Curreli, and F. Di Puccio, “AST: An OpenSim-based tool for the automatic scaling of generic musculoskeletal models,” *Comput Biol Med*, vol. 175, Jun. 2024, doi: 10.1016/j.compbiomed.2024.108524.

Appendix A

Ligaments	Spring stiffness (N)	Reference strain (-)	Optimized spring stiffness (N)
Superior medial collateral ligament	5500	0.01	-2.28%
Dorsal medial collateral ligament	2750	0.07	-6.73%
Posterior capsule medial	2000	0.07	-1.58%
Anterolateral ligament	4000	0.03	-8.83%
Lateral collateral ligament	6000	0.13	-9.05%
Posterior capsule	1000	0.07	-0.36%
Anterior Cruciate ligament	10000	0.06	-11.57%
Posterior Cruciate ligament	18000	-0.02	+55.47%
Medial patellar femoral ligament	6000	0.08	-12.08%
Lateral patellar femoral ligament	4000	0.06	-0.80%
Patellar tendon	12000	0	-22.47%
Muscles			
Vastus lateralis	4000	0	+66.46%
Vastus medialis	4000	0	-58.54%
Vastus Intermedius	4000	0	-58.39%
Vastus medialis oblique	4000	0	-58.54%
Contacts			
Femur - Medial Tibia plateau	25000	0	
Femur - Lateral Tibia plateau	25000	0	
Femur - Medial meniscus anterior horn	25000	0	
Femur - Medial meniscus posterior horn	25000	0	
Femur - Lateral meniscus anterior horn	25000	0	
Femur - Lateral meniscus posterior horn	25000	0	
Femur - Patella	25000	0	

Table 1: The soft tissue and contact conditions for the template model of the lower limb for the in-vivo and in-vitro validation experiments for rigid bone markers.

Ligament properties: D. L. Dejtiar, C. M. Dzialo, P. H. Pedersen, K. K. Jensen, M. K. Fleron, and M. S. Andersen, "Development and evaluation of a subject-specific lower limb model with an eleven-degrees-of-freedom natural knee model using magnetic resonance and biplanar x-ray imaging during a quasi-static lunge," *J Biomech Eng*, vol. 142, no. 6, Jun. 2020, doi: 10.1115/1.4044245.

Ligaments	Spring stiffness (N/mm)	Reference strain (-)
Lateral collateral ligament	57	0 at 110° flexion
Anterior medial collateral ligament	72.3	0 at 20° flexion
Posterior medial collateral ligament	52.2	0 at 98° flexion
Radial collateral ligament	15.5	0.02
Interosseus ligaments (4 bundles)	16.25	0.005
Dorsal distal radioulnar ligament	13.2	0.02
Volar distal radioulnar ligament	50.75	0.02
Oblique cord	65	0.005
Contacts		
Radius-Humerus	25	0
Ulna – Humerus trochlea medial part (2 contacts)	25	0
Ulna – Humerus trochlea lateral part (2 contacts)	25	0

970 *Table 2: The soft tissue and contact conditions for the template model of the upper limb for the in-vitro*

971 *validation experiments.*

972 Ligament parameters: J. P. Fisk and J. S. Wayne, “Development and validation of a computational musculoskeletal

973 model of the elbow and forearm,” Ann Biomed Eng, vol. 37, no. 4, pp. 803–812, Apr. 2009, doi: 10.1007/s10439-009-

974 9637-x.

975

Appendix B

In-vivo validation experiment (A): Healthy Lower Limb performing squats in a MRI scanner

		Number of rigid bone markers				
		3	**4**	**5**	**6**	**7**
Flexion-extension [°]	unoptimized	3.42 (0.79-6.76)	1.99 (0.15-3.34)	0.84 (0.13-2.25)	0.42 (0.07-1.11)	0.39 (0.04-0.82)
	optimized	1.91 (0.19-5.56)	1.19 (0.36-3.16)	0.56 (0.07-1.91)	0.25 (0.00-0.77)	0.16 (0.06-0.45)
Ab-adduction [°]	unoptimized	3.33 (0.13-8.25)	3.96 (0.11-7.85)	2.01 (0.26-8.23)	0.82 (0.24-1.30)	0.83 (0.11-1.40)
	optimized	0.83 (0.07-4.16)	0.79 (0.03-3.86)	3.12 (0.05-5.97)	0.29 (0.13-0.74)	0.33 (0.01-0.63)
Internal-external rotation [°]	unoptimized	9.54 (0.38-21.90)	1.82 (0.00-7.92)	1.04 (0.03-9.86)	1.60 (0.23-6.04)	0.78 (0.09-2.49)
	optimized	8.07 (0.57-21.06)	1.19 (0.20-11.21)	1.16 (0.36-8.68)	1.52 (0.48-4.76)	0.56 (0.15-2.14)
Medio-lateral translation [mm]	unoptimized	9.98 (2.68-13.32)	6.65 (0.93-10.89)	2.76 (0.23-6.35)	2.82 (0.10-6.10)	2.75 (0.28-5.79)
	optimized	7.31 (1.07-11.61)	5.50 (0.54-9.98)	1.52 (0.05-5.81)	2.10 (0.38-4.30)	1.68 (0.12-3.80)
Antero-posterior translation [mm]	unoptimized	2.31 (0.18-4.77)	2.05 (0.39-6.57)	1.22 (0.02-5.22)	1.01 (0.15-3.43)	0.98 (0.07-3.08)
	optimized	1.33 (0.03-4.64)	2.07 (0.13-6.09)	1.25 (0.01-5.10)	0.74 (0.04-3.37)	0.43 (0.01-2.63)
Supero-inferior translation [mm]	unoptimized	4.38 (0.98-9.03)	4.12 (0.50-6.87)	2.99 (0.77-4.25)	1.90 (0.39-2.70)	1.85 (0.31-2.73)
	optimized	3.12 (1.17-5.75)	2.51 (0.26-4.10)	1.72 (0.35-4.22)	1.12 (0.01-2.17)	1.02 (0.12-1.96)

Table 1: The median and range of the absolute errors on the estimation of the flexion-extension, ab-adduction, internal-external rotation, medio-lateral translation, anteroposterior translation and superoinferior translation for the 4 acquired positions for different numbers of rigid bone markers using both unoptimized and optimized ligament parameters.

In-vitro validation experiment (B): Cadaveric Lower Limb performing squats in a CT scanner

	Rigid bone markers						Skin			
	3	**4**	**5**	**6**	**7**	**Revolute (Bone)**	**Skin zones**	**Revolute (Skin)**	**OSSO**	**SKEL**
Flexion-extension [°]	5.38 (3.73-13.33)	4.13 (1.63-4.88)	1.49 (1.07-3.53)	1.90 (0.78-2.78)	0.59 (0.20-1.81)	2.72 (0.00-4.27)	0.85 (0.25-1.78)	7.29 (1.91-13.42)	9.59 (7.26-12.41)	3.19 (1.17-4.56)
Ab-adduction [°]	13.89 (6.57-23.41)	7.36 (6.72-8.07)	5.49 (2.68-7.82)	0.77 (0.42-1.24)	0.74 (0.40-1.10)	1.73 (0.15-2.63)	3.00 (0.15-4.96)	2.10 (0.55-2.56)	8.38 (3.64-13.82)	14.27 (6.38-17.72)
Internal-external rotation [°]	9.34 (7.29-17.18)	6.36 (4.68-10.37)	2.77 (0.94-9.38)	5.39 (2.69-13.34)	1.48 (0.61-3.08)	0.54 (0.25-4.06)	3.08 (0.27-9.91)	0.86 (0.18-3.15)	11.32 (8.83-13.26)	8.12 (7.49-9.63)
Medio-lateral translation [mm]	0.60 (0.35-3.43)	4.46 (2.17-7.23)	3.15 (1.47-5.62)	3.08 (1.48-8.83)	2.01 (0.41-2.92)	8.02 (0.73-23.61)	3.03 (1.04-6.05)	1.45 (0.56-4.68)	3.71 (2.76-4.98)	3.70 (2.75-4.97)
Superoinferior translation [mm]	0.91 (0.13-2.51)	1.50 (0.44-2.10)	0.75 (0.30-1.57)	1.13 (0.55-4.33)	0.84 (0.27-1.53)	0.69 (0.21-2.46)	3.52 (0.13-5.05)	3.01 (1.26-8.96)	17.84 (5.55-25.01)	17.82 (5.54-24.99)
Anteroposterior translation [mm]	2.50 (0.84-8.28)	3.99 (1.61-9.72)	2.47 (0.87-7.70)	2.89 (2.59-6.06)	2.59 (2.14-5.71)	10.90 (0.17-39.58)	1.75 (0.08-10.80)	2.37 (0.27-10.87)	10.16 (7.46-15.78)	10.14 (7.43-15.78)

Table 2: The median and range of the absolute errors on the estimation of the flexion-extension, ab-adduction, internal-external rotation, medio-lateral translation, anteroposterior translation and superoinferior translation for the 4 acquired positions for different numbers of rigid bone markers and skin zones for the soft tissue-integrated kinematic solver, revolute joint with bone and skin markers, OSSO and SKEL.

In-vitro validation experiment (C): Cadaveric Upper limb flexion-extension/pro-supination in a CT scanner

		Number of rigid bone markers							Number of skin markers			
		3	**4**	**5**	**6**	**7**	**8**	**9**	**4**	**7**	**10**	**Skin zones**
Humeroulnar	**Flexion-extension [°]**	3.78 (0.08-7.26)	4.61 (0.28-8.26)	5.27 (0.17-6.73)	1.44 (0.07-1.90)	1.09 (0.06-1.83)	1.18 (0.05-1.79)	1.14 (0.06-1.74)	6.92 (0.19-14.50)	4.38 (0.37-9.74)	4.97 (0.19-10.53)	3.70 (0.21-6.85)
	Axial rotation [°]	3.59 (0.39-9.30)	0.90 (0.15-1.20)	0.72 (0.20-1.40)	0.38 (0.01-0.76)	0.24 (0.00-0.76)	0.33 (0.06-0.81)	0.34 (0.04-0.75)	2.37 (0.16-5.49)	1.06 (0.07-2.99)	1.09 (0.22-2.35)	0.48 (0.08-2.00)
	Carrying angle [°]	1.76 (0.17-2.93)	4.24 (0.05-6.35)	4.55 (0.29-5.34)	1.25 (0.23-1.66)	1.25 (0.32-1.66)	1.28 (0.31-1.68)	1.23 (0.31-1.66)	4.17 (0.60-12.40)	5.32 (0.42-8.35)	6.35 (0.61-8.05)	3.45 (0.27-6.59)
	Medio-lateral translation [mm]	2.47 (0.09-4.10)	3.97 (0.61-4.61)	3.29 (0.71-4.48)	1.82 (0.17-2.81)	1.94 (0.71-2.72)	1.67 (0.70-2.78)	1.68 (0.67-2.76)	4.08 (0.40-5.10)	3.88 (2.05-5.33)	3.85 (0.59-4.98)	2.50 (0.71-4.75)
	Superoinferior translation [mm]	1.99 (0.40-3.42)	1.53 (0.40-3.55)	1.68 (0.578-2.42)	0.65 (0.02-2.56)	0.39 (0.04-2.67)	0.44 (0.00-2.76)	0.43 (0.07-2.80)	2.63 (0.69-7.79)	1.72 (0.02-10.13)	2.07 (0.18-7.48)	1.65 (0.21-5.00)
	Anteroposterior translation [mm]	2.06 (0.51-3.26)	1.96 (0.47-3.60)	2.03 (0.80-3.22)	1.67 (0.18-3.97)	0.78 (0.02-1.80)	0.81 (0.40-2.01)	0.75 (0.34-1.99)	2.13 (0.06-3.63)	1.89 (0.26-9.27)	1.71 (0.18-5.05)	2.76 (0.01-5.86)
Ulnoradial	**Orientation pro-supination axis [°]**	4.41 (0.37-10.60)	2.06 (0.04-8.99)	1.34 (0.10-4.27)	1.54 (0.03-3.56)	1.43 (0.04-3.49)	1.59 (0.38-3.67)	1.59 (0.00-3.72)	5.42 (1.27-18.34)	4.67 (0.06-23.00)	4.07 (0.08-13.00)	3.78 (1.47-7.53)
	Flexion-extension [°]	2.00 (0.49-8.98)	2.05 (0.21-5.27)	1.59 (0.05-4.14)	1.48 (0.51-3.33)	1.55 (0.26-3.28)	1.81 (0.17-3.37)	1.42 (0.21-3.49)	7.85 (0.91-23.28)	1.77 (0.40-14.59)	5.93 (0.87-9.82)	2.94 (0.03-10.81)
	Pro-supination [°]	3.09 (0.32-10.63)	0.99 (0.05-6.10)	0.60 (0.05-2.21)	0.84 (0.07-3.37)	0.92 (0.01-2.32)	1.09 (0.09-2.48)	1.13 (0.10-2.57)	3.07 (1.04-10.92)	1.85 (0.29-20.15)	1.50 (0.05-14.76)	2.94 (1.44-4.53)
	Superoinferior translation [mm]	0.96 (0.13-2.00)	1.14 (0.01-2.28)	1.11 (0.13-2.32)	0.40 (0.07-2.19)	0.32 (0.04-1.16)	0.31 (0.02-1.15)	0.40 (0.12-1.08)	1.87 (0.57-3.88)	1.98 (0.98-4.02)	1.50 (0.37-3.61)	0.72 (0.12-3.60)
	Mediolateral translation [mm]	1.13 (0.31-3.48)	1.16 (0.62-3.35)	1.16 (0.66-3.43)	1.47 (0.53-3.48)	1.29 (0.87-2.35)	1.25 (0.86-2.36)	1.22 (0.73-2.34)	1.24 (0.18-2.11)	1.96 (0.11-3.66)	1.21 (0.23-3.93)	2.04 (0.03-4.24)
	Anteroposterior translation [mm]	0.98 (0.09-2.97)	0.85 (0.23-3.07)	2.28 (0.31-3.96)	1.96 (0.55-4.07)	0.67 (0.40-2.68)	0.80 (0.39-2.60)	0.75 (0.33-2.31)	0.72 (0.23-2.24)	1.22 (0.15-2.80)	0.89 (0.07-2.75)	1.59 (0.19-3.03)

991 *Table 3: The median and range of the absolute errors on the estimation of the humeroulnar and ulnoradial angles and translations for the 11*

992 *acquired positions for different sets of rigid bone markers and skin markers.*

993